

Numerical Analysis of a Variable-Order Time-Fractional Incompressible Magnetohydrodynamics System

Abdumauvlen Berdyshev^{1,2}, Dossan Baigereyev^{1,3}, Aibek Bakishev^{1,3},
Nurlana Alimbekova^{1,3}, Talgat Farkhadov¹

¹Institute of Information and Computational Technologies, Almaty, Kazakhstan

²Abai Kazakh National Pedagogical University, Almaty, Kazakhstan

³Sarsen Amanzholov East Kazakhstan University, Ust-Kamenogorsk, Kazakhstan

April 28, 2026

Abstract

We consider an incompressible magnetohydrodynamics (MHD) model in which the classical first-order time derivatives in the momentum and magnetic induction equations are replaced by variable-order Caputo time-fractional derivatives. This formulation allows the memory effect to vary during the evolution and represents a time-fractional generalization of the incompressible MHD system with nonstationary memory. To approximate the problem, we use a fully discrete scheme combining a finite element discretization in space with an L1-type approximation of the variable-order Caputo operators in time. For this discretization, stability is obtained using corrected discrete memory functionals adapted to the variable-order fractional terms. Convergence is proved by showing that the kernels generated by the variable-order L1 approximation satisfy the assumptions of an abstract discrete fractional Grönwall theorem, which is then applied to the coupled MHD system. The numerical study consists of four parts. First, representative order profiles are used to examine temporal convergence. Second, consistency with the classical incompressible MHD equations is studied in the limit as the fractional orders approach one, using norms of solution differences together with deviations in kinetic and magnetic energies. Third, the influence of the variable-order fractional terms on nonlinear evolution is investigated through the periodic divergence-free vortex benchmark, with comparisons based on energy and enstrophy histories, divergence errors, Reynolds-number dependence, and changes in time-integrated diagnostics. Fourth, parameter-space maps are used to show how the parameters defining the variable orders affect global indicators. The results show that the variable fractional orders can noticeably affect the evolution of the energy, enstrophy, and current enstrophy even when the Reynolds number is fixed.

1 Introduction

Magnetohydrodynamics (MHD) plays a fundamental role in describing processes occurring in electrically conducting media such as plasma, liquid metals, electrolytes and astrophysical objects. In recent decades, MHD problems have found wide application in plasma physics, geophysics, metallurgy, nuclear energy, biomedicine, and engineering sciences [17, 38, 44]. The study of MHD processes allows for a better understanding of the mechanisms of interaction between a magnetic field and a fluid flow, which is key in the development of magnetic cooling technologies, control of plasma installations, and in modeling natural phenomena such as solar flares and geomagnetic storms [3, 9, 37].

On the other hand, many physical processes, including diffusion, heat transfer, and viscoelastic flow, exhibit memory and heredity effects that cannot be adequately described using classical

differential models. To take these properties into account, fractional calculus based on derivatives and integrals of arbitrary (non-integer) order is effectively used [7, 12, 14, 19, 34, 36]. Due to their ability to describe processes with anomalous diffusion, subdiffusion and superdiffusion, fractional derivatives are successfully used in modeling various real phenomena – from charge and heat transfer to deformation of viscoelastic materials [2, 16, 32, 33, 47, 49]. Recently, fractional differential models have come under consideration, in which the order of the fractional derivative depends on time, a spatial variable, or the desired solution [4, 6, 35, 48]. The variable order allows describing situations where the intensity of hereditary effects and anomalous diffusion changes in time or space, which is especially characteristic of complex MHD processes with transitions between different flow regimes.

The combination of MHD equations and fractional calculus has motivated an active research direction, namely, MHD-related models with fractional derivatives. Such models are used to incorporate nonlocal temporal effects, and in some cases nonlocal constitutive behavior, beyond the classical formulation. For example, in [5], the Atangana–Baleanu time-fractional operator with a Mittag–Leffler kernel was used in an MHD viscous-fluid model with slip and Newtonian heating. Arif et al. [8] studied a fractional MHD flow of a generalized Oldroyd-B fluid with couple stresses, heat transfer, and mass transfer, while Asjad et al. [10] numerically investigated a fractional MHD Maxwell nanofluid flow between coaxial cylinders. These works illustrate the growing use of fractional operators in MHD flow models, although they differ substantially from the incompressible variable-order system considered in the present paper.

Since closed-form solutions are rarely available for fractional MHD models, considerable attention has been paid to numerical methods. In [11, 18, 31, 39, 45], various approaches are proposed, including finite difference, finite volume, spectral element, and finite element methods. These methods made it possible to successfully model convection and heat-transfer processes in electrically conducting liquids with fractional derivatives. For example, Shen et al. [46] studied the unsteady flow of fractional Maxwellian nanofluid in a magnetic field, and Zhao et al. [53] analyzed a spatially fractional MHD free-convection problem with Soret and Dufour effects. The paper [30] considers a Maxwell fluid under MHD conditions, incorporating modified dynamic viscosity and effects such as Hall current and Joule heating, and employs an L1-type scheme coupled with a spectral collocation method. In [15], a system of fractional MHD equations in a three-dimensional unbounded domain under Dirichlet boundary conditions is investigated, and decay estimates for weak solutions in the L^2 -norm are derived.

The aim of this paper is to develop, analyze, and test a fully discrete numerical scheme for incompressible magnetohydrodynamics with variable-order Caputo time-fractional derivatives. Particular attention is given to the influence of time-dependent fractional orders on transient MHD behavior and to the recovery of the classical incompressible MHD model in the limit as the orders approach unity. The numerical study is therefore used not only to assess the reliability of the discretization, but also to examine how different order profiles affect the evolution of standard diagnostic quantities.

Most existing studies on time-fractional MHD models consider constant-order formulations and often focus on analytical or computational investigations in reduced flow configurations [1, 8, 43]. By comparison, studies incorporating variable- or distributed-order memory effects in MHD appear much less frequently [26, 27, 42] and, to our knowledge, are generally not accompanied by a fully discrete numerical analysis for the incompressible MHD system considered here. In particular, it remains insufficiently understood how the temporal profile of the fractional order influences standard MHD diagnostics and whether a numerical discretization consistently recovers the classical MHD behavior as the fractional orders approach unity. From the analytical point of view, the variable-order formulation introduces an additional difficulty because the discrete memory kernels depend on the current time level and must be treated within a coupled incompressible MHD system. Consequently, the convergence proof requires more than a direct extension of the constant-order analysis: one must verify that the kernels generated by

the variable-order L1 discretization satisfy the assumptions of the abstract discrete fractional Grönwall theorem [28] used in the error analysis.

In view of these considerations, the main contributions of this paper are as follows.

(1) We formulate a variable-order time-fractional generalization of the incompressible MHD equations by replacing the classical first-order time derivatives in the momentum and magnetic induction equations with Caputo derivatives of time-dependent orders $\alpha(t), \beta(t) \in (0, 1)$, respectively. This formulation allows the temporal memory effect to vary during the evolution and thereby captures MHD dynamics with nonstationary relaxation behavior.

(2) We construct a fully discrete numerical method for the coupled incompressible MHD system by combining a finite element approximation in space with an L1-type discretization in time for the variable-order Caputo operators.

(3) For the fully discrete scheme, we establish stability and derive a convergence estimate. The stability estimate is obtained using a corrected discrete memory functional. In the convergence analysis, we verify that the discrete kernels generated by the variable-order L1 approximation satisfy the assumptions required for applying the abstract discrete fractional Grönwall theorem of [28] to the finite element–L1 scheme.

(4) We perform representative numerical tests to validate the method and investigate how time-dependent fractional orders affect the solution behavior. These include convergence studies for selected order profiles, a classical-limit test showing consistency with the standard incompressible MHD equations as $\alpha(t), \beta(t) \rightarrow 1$, and simulations of the periodic divergence-free vortex under several variable-order scenarios.

(5) We further examine the sensitivity of the model to the temporal memory profile through parameter-space maps for the order-function parameters, using global diagnostics to quantify how the evolution depends on the choice of the variable order.

The rest of the paper is organized as follows. Section 2 introduces the variable-order time-fractional incompressible magnetohydrodynamic model and summarizes the numerical method used for its discretization and implementation, and presents its rigorous analysis. Section 3 presents the computational results and analyzes how the variable-order Caputo time derivatives influence the flow dynamics across the considered numerical experiments, including verification tests and the variable-order fractional periodic divergence-free vortex benchmark. Section 4 discusses and summarizes the main findings, and Section 5 states the concluding remarks and outlines directions for future work.

2 Problem Formulation and Numerical Method

2.1 Problem Formulation

In this paper, we consider a variable-order time-fractional generalization of the incompressible magnetohydrodynamic equations in the domain $\Omega \times (0, T]$, where Ω is a bounded subdomain of \mathbb{R}^2 , and $T > 0$ is a finite time:

$$\rho_0 \theta^{\alpha(t)-1} {}^C D_t^{\alpha(t)} \mathbf{u} + \rho_0 (\mathbf{u} \cdot \nabla) \mathbf{u} = -\nabla P + \mu \nabla^2 \mathbf{u} + \frac{1}{\mu_0} (\nabla \times \mathbf{B}) \times \mathbf{B} + \mathbf{f} \quad \text{in } \Omega \times (0, T], \quad (1)$$

$$\theta^{\beta(t)-1} {}^C D_t^{\beta(t)} \mathbf{B} = \nabla \times (\mathbf{u} \times \mathbf{B}) + \eta \nabla^2 \mathbf{B} + \mathbf{g} \quad \text{in } \Omega \times (0, T], \quad (2)$$

$$\nabla \cdot \mathbf{u} = 0, \quad \nabla \cdot \mathbf{B} = 0 \quad \text{in } \Omega \times (0, T], \quad (3)$$

obtained from the classical incompressible MHD system (cf. [21]) by replacing the first-order time derivatives with Caputo derivatives of orders $\alpha(t), \beta(t) \in (0, 1)$ that depend on the observation time t ,

$$({}^C D_t^{\nu(t)} f)(t) = \frac{1}{\Gamma(1-\nu(t))} \int_0^t \frac{\partial_s f(s)}{(t-s)^{\nu(t)}} ds, \quad 0 < \nu(t) < 1, \quad t \in [0, T], \quad (4)$$

where $\nu \in \{\alpha, \beta\}$. Since ${}^C D_t^{\nu(t)}$ carries the physical dimension $[s]^{-\nu(t)}$, we multiply it by $\theta^{\nu(t)-1}$ so that the fractional term has the same dimension as a first-order time derivative (cf. [50]). When $\nu(t) \rightarrow 1$, this prefactor tends to 1, and the classical model is recovered. In particular, $\alpha(t) \equiv 1$ and $\beta(t) \equiv 1$ reduce the system to the standard incompressible MHD equations [21].

In Eqs. (1)–(3), \mathbf{u} denotes the velocity, \mathbf{B} is the magnetic field, P is the pressure, ρ_0 is the density, μ is the dynamic viscosity, η is the magnetic diffusion, μ_0 is magnetic force scaling, $\mathbf{f}(\mathbf{x}, t)$ and $\mathbf{g}(\mathbf{x}, t)$ are source terms, and $\mathbf{x} \in \mathbb{R}^2$. Eqs. (1)–(3) are supplemented with initial conditions

$$\mathbf{u} = \mathbf{u}_0, \quad \mathbf{B} = \mathbf{B}_0 \quad \text{in } \bar{\Omega} \times \{0\},$$

satisfying the conditions $\nabla \cdot \mathbf{u}_0 = 0$, $\nabla \cdot \mathbf{B}_0 = 0$, and with one of the following boundary conditions:

(i) homogeneous Dirichlet boundary conditions,

$$\mathbf{u} = \mathbf{0}, \quad \mathbf{B} = \mathbf{0} \quad \text{on } \partial\Omega \times (0, T];$$

(ii) periodic boundary conditions.

The curl and cross product operations are understood through the standard embedding of planar vector fields into \mathbb{R}^3 , namely $\mathbf{u} = (u_1, u_2, 0)$ and $\mathbf{B} = (B_1, B_2, 0)$, so that, for example, $\nabla \times \mathbf{B} = (0, 0, \partial_{x_1} B_2 - \partial_{x_2} B_1)$.

We introduce characteristic scales S_0 (length), U_0 (velocity), $T_0 = \theta = S_0/U_0$ (time), $B_0 = U_0 \sqrt{\rho_0 \mu_0}$ (magnetic field), and $p_0 = \rho_0 U_0^2$ (pressure), and define dimensionless variables $\mathbf{x}^* = \frac{\mathbf{x}}{S_0}$, $t^* = \frac{t}{T_0}$, $\mathbf{u}^* = \frac{\mathbf{u}}{U_0}$, $P^* = \frac{P}{p_0}$, and $\mathbf{B}^* = \frac{\mathbf{B}}{B_0}$.

Using the scaling property of the Caputo derivative,

$$\begin{aligned} ({}^C D_t^{\alpha(t)} \mathbf{u})(t) &= U_0 T_0^{-\alpha(T_0 t^*)} ({}^C D_{t^*}^{\alpha(T_0 t^*)} \mathbf{u}^*)(t^*), \\ ({}^C D_t^{\beta(t)} \mathbf{B})(t) &= B_0 T_0^{-\beta(T_0 t^*)} ({}^C D_{t^*}^{\beta(T_0 t^*)} \mathbf{B}^*)(t^*), \end{aligned}$$

we obtain the dimensionless system

$${}^C D_{t^*}^{\alpha^*(t^*)} \mathbf{u}^* + (\mathbf{u}^* \cdot \nabla^*) \mathbf{u}^* = -\nabla^* P^* + \frac{1}{\text{Re}} \nabla^{*2} \mathbf{u}^* + (\nabla^* \times \mathbf{B}^*) \times \mathbf{B}^* + \mathbf{f}^*, \quad (5)$$

$${}^C D_{t^*}^{\beta^*(t^*)} \mathbf{B}^* = \nabla^* \times (\mathbf{u}^* \times \mathbf{B}^*) + \frac{1}{\text{Rm}} \nabla^{*2} \mathbf{B}^* + \mathbf{g}^*, \quad (6)$$

$$\nabla^* \cdot \mathbf{u}^* = 0, \quad \nabla^* \cdot \mathbf{B}^* = 0, \quad (7)$$

where $\alpha^*(t^*) = \alpha(T_0 t^*)$, $\beta^*(t^*) = \beta(T_0 t^*)$, $\text{Re} = \frac{\rho_0 U_0 S_0}{\mu}$, $\text{Rm} = \frac{U_0 S_0}{\eta}$, $\mathbf{f}^* = \frac{S_0}{\rho_0 U_0^2} \mathbf{f}$, and $\mathbf{g}^* = \frac{T_0}{U_0 \sqrt{\rho_0 \mu_0}} \mathbf{g}$. For convenience, we henceforth omit the asterisks from all dimensionless variables and operators, and write $\alpha(t)$, $\beta(t)$ for the dimensionless order functions.

We now derive the variational (weak) formulation associated with the non-dimensional system (5)–(7). Throughout the paper, we use standard notation for Sobolev spaces. The usual spaces $H^s(\Omega)$ and $W^{k,p}(\Omega)$ are equipped with their standard norms. In particular, $\|\cdot\|$ denotes the norm in $L^2(\Omega)$, and $\|\cdot\|_{L^p}$ denotes the norm in $L^p(\Omega)$. We introduce the pressure space $\mathcal{Q} = L_0^2(\Omega) = \{q \in L^2(\Omega) : \int_{\Omega} q \, d\mathbf{x} = 0\}$. For the velocity and magnetic field, we introduce the corresponding function spaces according to the boundary conditions under consideration. In the case of homogeneous Dirichlet boundary conditions, we take $\mathcal{V} = H_0^1(\Omega)^2$, $\mathcal{C} = H_0^1(\Omega)^2$. In the periodic case, we take $\mathcal{V} = H_{\text{per}}^1(\Omega)^2$, $\mathcal{C} = H_{\text{per}}^1(\Omega)^2$, where $H_{\text{per}}^1(\Omega)^2$ denotes the corresponding periodic Sobolev space.

To obtain a convenient form of the pressure and coupling terms, we employ the standard vector identities

$$(\nabla \times \mathbf{B}) \times \mathbf{B} = (\mathbf{B} \cdot \nabla) \mathbf{B} - \nabla \left(\frac{1}{2} |\mathbf{B}|^2 \right), \quad \nabla \times (\mathbf{u} \times \mathbf{B}) = (\mathbf{B} \cdot \nabla) \mathbf{u} - (\mathbf{u} \cdot \nabla) \mathbf{B}$$

under the constraints (7), and introduce the total pressure $p = P + \frac{1}{2} |\mathbf{B}|^2$. For $\mathbf{a}, \mathbf{b}, \mathbf{w} \in H^1(\Omega)^2$ we further define the trilinear form

$$\ell(\mathbf{a}; \mathbf{b}, \mathbf{w}) = ((\mathbf{a} \cdot \nabla) \mathbf{b}, \mathbf{w}) + \frac{1}{2} ((\nabla \cdot \mathbf{a}) \mathbf{b}, \mathbf{w}), \quad (8)$$

where (\cdot, \cdot) denotes the $L^2(\Omega)$ inner product. Under homogeneous Dirichlet or periodic boundary conditions, integration by parts yields the equivalent representation

$$\ell(\mathbf{a}; \mathbf{b}, \mathbf{w}) = \frac{1}{2} ((\mathbf{a} \cdot \nabla) \mathbf{b}, \mathbf{w}) - \frac{1}{2} ((\mathbf{a} \cdot \nabla) \mathbf{w}, \mathbf{b}), \quad (9)$$

and therefore

$$\ell(\mathbf{a}; \mathbf{b}, \mathbf{b}) = 0, \quad \ell(\mathbf{a}; \mathbf{b}, \mathbf{w}) = -\ell(\mathbf{a}; \mathbf{w}, \mathbf{b}). \quad (10)$$

Then the weak formulation reads:

Problem 2.1. Find $(\mathbf{u}, p, \mathbf{B}) \in \mathcal{V} \times \mathcal{Q} \times \mathcal{C}$ such that, for all $(\mathbf{v}, q, \mathbf{C}) \in \mathcal{V} \times \mathcal{Q} \times \mathcal{C}$,

$$\left({}^C D_t^{\alpha(t)} \mathbf{u}, \mathbf{v} \right) + \frac{1}{\text{Re}} (\nabla \mathbf{u}, \nabla \mathbf{v}) + \ell(\mathbf{u}; \mathbf{u}, \mathbf{v}) - \ell(\mathbf{B}; \mathbf{B}, \mathbf{v}) - (p, \nabla \cdot \mathbf{v}) = \langle \mathbf{f}, \mathbf{v} \rangle, \quad (11)$$

$$\left({}^C D_t^{\beta(t)} \mathbf{B}, \mathbf{C} \right) + \frac{1}{\text{Rm}} (\nabla \mathbf{B}, \nabla \mathbf{C}) + \ell(\mathbf{u}; \mathbf{B}, \mathbf{C}) - \ell(\mathbf{B}; \mathbf{u}, \mathbf{C}) = \langle \mathbf{g}, \mathbf{C} \rangle, \quad (12)$$

$$(\nabla \cdot \mathbf{u}, q) = 0. \quad (13)$$

The magnetic solenoidal condition $\nabla \cdot \mathbf{B} = 0$ is understood as part of the continuous MHD model, but it is not introduced here as a separate weak equation. Similar H^1 -conforming variational formulations for the magnetic field have been used in finite element analyses of incompressible MHD (cf. [21]).

2.2 Numerical Method

To discretize the problem in time, we introduce the partition \mathcal{I}_N of the time interval $[0, T]$ by the points $t_n = n\tau$, $\tau > 0$, $n = 0, 1, \dots, N$, so that $N\tau = T$. Denote $\phi^n = \phi(\cdot, t_n)$. Further, we approximate the variable-order Caputo fractional derivative (4) using the formula [29]

$$\left({}^C D_t^{\nu(t_n)} \phi \right) (t_n) = \Delta_\tau^{\nu(t_n)} \phi^n + O(\tau), \quad 0 < \nu(t_n) < 1 \quad (14)$$

with

$$\Delta_\tau^{\nu(t_n)} \phi^n = \frac{1}{\tau} \left(b_{n,n}^{(\nu)} \phi^n - \sum_{k=1}^{n-1} \left(b_{n,k+1}^{(\nu)} - b_{n,k}^{(\nu)} \right) \phi^k - b_{n,1}^{(\nu)} \phi^0 \right) = \frac{1}{\tau} \sum_{k=1}^n b_{n,k}^{(\nu)} \left(\phi^k - \phi^{k-1} \right), \quad (15)$$

where

$$b_{n,k}^{(\nu)} = \frac{1}{\Gamma(2 - \nu(t_n))} \left((t_n - t_{k-1})^{1-\nu(t_n)} - (t_n - t_k)^{1-\nu(t_n)} \right). \quad (16)$$

Using (14), we rewrite Problem 2.1 as follows.

Problem 2.2. Let the solutions $\mathbf{u}^i \in \mathcal{V}$, $\mathbf{B}^i \in \mathcal{C}$ be known at time levels $i = 0, \dots, n-1$. Find $(\mathbf{u}^n, p^n, \mathbf{B}^n) \in \mathcal{V} \times \mathcal{Q} \times \mathcal{C}$, satisfying the following identities for all $(\mathbf{v}, q, \mathbf{C}) \in \mathcal{V} \times \mathcal{Q} \times \mathcal{C}$:

$$\begin{aligned} \left(\Delta_\tau^{\alpha(t_n)} \mathbf{u}^n, \mathbf{v} \right) + \frac{1}{\text{Re}} (\nabla \mathbf{u}^n, \nabla \mathbf{v}) + \ell(\mathbf{u}^n; \mathbf{u}^n, \mathbf{v}) - \ell(\mathbf{B}^n; \mathbf{B}^n, \mathbf{v}) \\ - (p^n, \nabla \cdot \mathbf{v}) = \langle \mathbf{f}^n, \mathbf{v} \rangle - (\mathbf{r}_1^n, \mathbf{v}), \end{aligned} \quad (17)$$

$$\begin{aligned} \left(\Delta_\tau^{\beta(t_n)} \mathbf{B}^n, \mathbf{C} \right) + \frac{1}{\text{Rm}} (\nabla \mathbf{B}^n, \nabla \mathbf{C}) + \ell(\mathbf{u}^n; \mathbf{B}^n, \mathbf{C}) \\ - \ell(\mathbf{B}^n; \mathbf{u}^n, \mathbf{C}) = \langle \mathbf{g}^n, \mathbf{C} \rangle - (\mathbf{r}_2^n, \mathbf{C}), \end{aligned} \quad (18)$$

$$(\nabla \cdot \mathbf{u}^n, q) = 0, \quad (19)$$

where

$$\begin{aligned} \mathbf{r}_1^n &= ({}^C D_t^{\alpha(t_n)} \mathbf{u})(t_n) - \Delta_\tau^{\alpha(t_n)} \mathbf{u}^n, \\ \mathbf{r}_2^n &= ({}^C D_t^{\beta(t_n)} \mathbf{B})(t_n) - \Delta_\tau^{\beta(t_n)} \mathbf{B}^n. \end{aligned}$$

Let us further introduce a triangulation \mathfrak{T}_h of Ω with the discretization parameter $h > 0$, and let $\mathcal{V}_h \subset \mathcal{V}$, $\mathcal{Q}_h \subset \mathcal{Q}$, and $\mathcal{C}_h \subset \mathcal{C}$ be conforming finite element spaces. We define the numerical scheme as follows.

Problem 2.3. Suppose that the discrete solutions $\mathbf{u}_h^i \in \mathcal{V}_h$, $\mathbf{B}_h^i \in \mathcal{C}_h$ are known at time levels $i = 0, \dots, n-1$. Find $(\mathbf{u}_h^n, p_h^n, \mathbf{B}_h^n) \in \mathcal{V}_h \times \mathcal{Q}_h \times \mathcal{C}_h$ satisfying the following identities for all $(\mathbf{v}_h, q_h, \mathbf{C}_h) \in \mathcal{V}_h \times \mathcal{Q}_h \times \mathcal{C}_h$:

$$\begin{aligned} \left(\Delta_\tau^{\alpha(t_n)} \mathbf{u}_h^n, \mathbf{v}_h \right) + \frac{1}{\text{Re}} (\nabla \mathbf{u}_h^n, \nabla \mathbf{v}_h) + \ell(\mathbf{u}_h^n; \mathbf{u}_h^n, \mathbf{v}_h) - \ell(\mathbf{B}_h^n; \mathbf{B}_h^n, \mathbf{v}_h) \\ - (p_h^n, \nabla \cdot \mathbf{v}_h) + \zeta (\nabla \cdot \mathbf{u}_h^n, \nabla \cdot \mathbf{v}_h) = \langle \mathbf{f}^n, \mathbf{v}_h \rangle, \end{aligned} \quad (20)$$

$$\begin{aligned} \left(\Delta_\tau^{\beta(t_n)} \mathbf{B}_h^n, \mathbf{C}_h \right) + \frac{1}{\text{Rm}} (\nabla \mathbf{B}_h^n, \nabla \mathbf{C}_h) + \ell(\mathbf{u}_h^n; \mathbf{B}_h^n, \mathbf{C}_h) \\ - \ell(\mathbf{B}_h^n; \mathbf{u}_h^n, \mathbf{C}_h) + \chi (\nabla \cdot \mathbf{B}_h^n, \nabla \cdot \mathbf{C}_h) = \langle \mathbf{g}^n, \mathbf{C}_h \rangle, \end{aligned} \quad (21)$$

$$(\nabla \cdot \mathbf{u}_h^n, q_h) = 0. \quad (22)$$

Since the velocity and magnetic field are approximated in H^1 -conforming finite element spaces, the constraints (7) are not enforced pointwise at the discrete level. To improve the control of these constraints, we augment the momentum and magnetic equations by the consistent stabilization terms $\zeta (\nabla \cdot \mathbf{u}_h^n, \nabla \cdot \mathbf{v}_h)$ and $\chi (\nabla \cdot \mathbf{B}_h^n, \nabla \cdot \mathbf{C}_h)$, where $\zeta \geq 0$ and $\chi \geq 0$ are stabilization parameters. These terms vanish for divergence-free exact solutions and therefore do not affect the consistency of the method. Their role is to penalize discrete divergence errors and improve mass conservation and magnetic solenoidality in the numerical approximation.

2.3 Stability and Convergence Analysis

In this section, we establish the stability and convergence of the fully discrete finite element–L1 scheme. The main analytical difficulty arises from the variable-order L1 discretization of the Caputo derivatives. In contrast to the constant-order case, the discrete coefficients depend on the current time level t_n , so the resulting memory kernels vary with n and cannot be handled by the standard fixed-order analysis. In the present problem, this issue must be handled within the nonlinear coupled structure of the incompressible MHD system. To overcome it, the stability analysis is based on the corrected discrete memory functional $\mathcal{E}_{\phi, n}^{(\nu)}$ defined below, which provides a suitable estimate even when the fractional order function $\nu(t)$ is non-monotone. For the convergence proof, we additionally verify that the kernels generated by the variable-order L1 approximation satisfy the assumptions of the abstract discrete fractional Grönwall theorem [28] used to bound the fully discrete error sequence.

Assumption 2.4. Let l and m be the exponents determined by the approximation properties of the finite element spaces for the velocity and magnetic field, respectively. Assume that the exact solution satisfies

$$\begin{aligned} \mathbf{u} &\in L^\infty(0, T; H^{l+1}(\Omega)^2) \cap L^\infty(0, T; W^{1, \infty}(\Omega)^2), & \partial_t \mathbf{u} &\in L^\infty(0, T; H^{l+1}(\Omega)^2), \\ \mathbf{B} &\in L^\infty(0, T; H^{m+1}(\Omega)^2) \cap L^\infty(0, T; W^{1, \infty}(\Omega)^2), & \partial_t \mathbf{B} &\in L^\infty(0, T; H^{m+1}(\Omega)^2), \end{aligned}$$

and that \mathbf{u} and \mathbf{B} satisfy the prescribed boundary conditions. In the periodic case, we additionally assume that the velocity and magnetic field have zero spatial mean.

Furthermore, we assume that $\mathbf{f}, \mathbf{g} \in L^2(0, T; H^{-1}(\Omega)^2)$.

Assumption 2.5. Assume that $\alpha, \beta \in C[0, T]$, and

$$0 < \alpha_* \leq \alpha(t) \leq \alpha^* < 1, \quad 0 < \beta_* \leq \beta(t) \leq \beta^* < 1.$$

We will repeatedly use several standard inequalities in the analysis. In the case of homogeneous Dirichlet boundary conditions, the Poincaré inequality holds on the discrete velocity and magnetic field spaces since they are conforming subspaces of $H_0^1(\Omega)^2$. In the periodic case, the corresponding estimate is used on the subspace of periodic functions with zero spatial mean. Therefore, in both cases there exists a constant $C > 0$, independent of h , such that

$$\|\mathbf{v}_h\| \leq C\|\nabla\mathbf{v}_h\|, \quad \|\mathbf{C}_h\| \leq C\|\nabla\mathbf{C}_h\|$$

for all $\mathbf{v}_h \in \mathcal{V}_h$ and $\mathbf{C}_h \in \mathcal{C}_h$.

Under the same assumptions, we use the two-dimensional Ladyzhenskaya inequality

$$\|\mathbf{v}\|_{L^4} \leq C\|\mathbf{v}\|^{1/2}\|\nabla\mathbf{v}\|^{1/2}$$

for $\mathbf{v} \in H_0^1(\Omega)^2$ in the homogeneous Dirichlet case and for $\mathbf{v} \in H_{\text{per}}^1(\Omega)^2$ with zero spatial mean in the periodic case.

We also use the inverse inequality for discrete functions

$$\|\mathbf{v}_h\|_{L^4} \leq Ch^{-1/2}\|\mathbf{v}_h\|, \quad \|\nabla\mathbf{v}_h\| \leq Ch^{-1}\|\mathbf{v}_h\|.$$

We first establish some basic properties of the coefficients $b_{n,k}^{(\nu)}$ in (16).

Lemma 2.6. Let $0 < \nu_* \leq \nu(t) \leq \nu^* < 1$, $t \in [0, T]$. Then the coefficients $b_{n,k}^{(\nu)}$ have the following properties:

$$b_{n,n}^{(\nu)} > b_{n,n-1}^{(\nu)} > \dots > b_{n,1}^{(\nu)} > 0, \quad (23)$$

$$\sum_{k=1}^n b_{n,k}^{(\nu)} = \frac{t_n^{1-\nu(t_n)}}{\Gamma(2-\nu(t_n))}, \quad t_n \in \mathcal{I}_N, \quad (24)$$

$$\sum_{k=1}^n b_{k,1}^{(\nu)} \leq \gamma, \quad \gamma = \begin{cases} \frac{T^{1-\nu^*}}{1-\nu^*}, & T \leq 1, \\ \frac{1}{1-\nu^*} + \frac{T^{1-\nu_*-1}}{1-\nu_*}, & T > 1. \end{cases} \quad (25)$$

Proof. Eq. (24) is verified directly. Let $\nu_n = \nu(t_n)$, $t_n \in \mathcal{I}_N$. Since the function $f(x) = x^{1-\nu_n}$ is increasing and concave on $(0, \infty)$, the increments $f(m+1) - f(m) = (m+1)^{1-\nu_n} - m^{1-\nu_n}$, $m \geq 0$, are positive and decrease as m increases. Taking $m = n - k$, and noting that $b_{n,k}^{(\nu)}$ is obtained from these increments by multiplication by the positive factor $\frac{\tau^{1-\nu_n}}{\Gamma(2-\nu_n)}$, we obtain (23).

Finally, by the definition of $b_{k,1}^{(\nu)}$, for each $k \geq 1$,

$$b_{k,1}^{(\nu)} = \frac{t_k^{1-\nu_k} - t_{k-1}^{1-\nu_k}}{\Gamma(2-\nu_k)} = \frac{1}{\Gamma(1-\nu_k)} \int_{t_{k-1}}^{t_k} s^{-\nu_k} ds \leq \int_{t_{k-1}}^{t_k} s^{-\nu_k} ds,$$

since $\Gamma(1-\nu_k) > 1$ as $1-\nu_k \in (0, 1)$.

If $T \leq 1$, then $0 < s \leq t_n \leq T \leq 1$. Since $s^{-\alpha}$ is increasing with respect to α for $0 < s \leq 1$, we have $s^{-\nu_k} \leq s^{-\nu^*}$. Therefore,

$$\sum_{k=1}^n b_{k,1}^{(\nu)} \leq \int_0^{t_n} s^{-\nu^*} ds = \frac{t_n^{1-\nu^*}}{1-\nu^*} \leq \frac{T^{1-\nu^*}}{1-\nu^*}.$$

Now suppose $T > 1$. If $t_n \leq 1$, then the same argument gives

$$\sum_{k=1}^n b_{k,1}^{(\nu)} \leq \frac{1}{1-\nu^*} \leq \frac{1}{1-\nu^*} + \frac{T^{1-\nu^*} - 1}{1-\nu^*}.$$

If $t_n > 1$, then on $(0, 1]$, we use $s^{-\nu_k} \leq s^{-\nu^*}$, while on $[1, t_n]$, we use $s^{-\nu_k} \leq s^{-\nu^*}$ since $s^{-\alpha}$ is decreasing with respect to α for $s \geq 1$. Therefore,

$$\sum_{k=1}^n b_{k,1}^{(\nu)} \leq \int_0^1 s^{-\nu^*} ds + \int_1^{t_n} s^{-\nu^*} ds = \frac{1}{1-\nu^*} + \frac{t_n^{1-\nu^*} - 1}{1-\nu^*} \leq \frac{1}{1-\nu^*} + \frac{T^{1-\nu^*} - 1}{1-\nu^*},$$

since $t_n \leq T$. \square

Now we derive a discrete energy inequality for the variable-order L1-Caputo operator. For this purpose, we introduce a corrected discrete memory functional $\mathcal{E}_{\phi,n}^{(\nu)} = \Theta_{\phi,n}^{(\nu)} - R_{\phi,n}^{(\nu)}$ which will be used in the stability analysis.

Lemma 2.7. *Given the sequence $\{\phi^n\}_{n \geq 0}$, $\phi^n \in L^2(\Omega)$, define*

$$\Theta_{\phi,0}^{(\nu)} = 0, \quad \Theta_{\phi,n}^{(\nu)} = \frac{1}{2} \sum_{k=1}^n b_{n,k}^{(\nu)} \|\phi^k\|^2, \quad n \geq 1, \quad (26)$$

$$\delta_{n,k}^{(\nu)} = b_{n,k+1}^{(\nu)} - b_{n-1,k}^{(\nu)}, \quad \left(\delta_{n,k}^{(\nu)}\right)_+ = \max\{\delta_{n,k}^{(\nu)}, 0\}, \quad (27)$$

$$R_{\phi,0}^{(\nu)} = R_{\phi,1}^{(\nu)} = 0, \quad R_{\phi,n}^{(\nu)} = \frac{1}{2} \sum_{j=2}^n \sum_{k=1}^{j-1} \left(\delta_{j,k}^{(\nu)}\right)_+ \|\phi^k\|^2, \quad n \geq 2, \quad (28)$$

and

$$\mathcal{E}_{\phi,n}^{(\nu)} = \Theta_{\phi,n}^{(\nu)} - R_{\phi,n}^{(\nu)}. \quad (29)$$

Then for all $n \geq 1$,

$$\left(\Delta_{\tau}^{\nu(t_n)} \phi^n, \phi^n\right) \geq \frac{1}{\tau} \left(\mathcal{E}_{\phi,n}^{(\nu)} - \mathcal{E}_{\phi,n-1}^{(\nu)}\right) - \frac{1}{2\tau} b_{n,1}^{(\nu)} \|\phi^0\|^2. \quad (30)$$

Proof. For fixed n , the order $\nu(t_n)$ is fixed. Hence by (15), (23), summation by parts, and Young's inequality, we obtain

$$\begin{aligned} \left(\Delta_{\tau}^{\nu(t_n)} \phi^n, \phi^n\right) &= \frac{1}{\tau} \left[b_{n,n}^{(\nu)} \|\phi^n\|^2 - \sum_{k=1}^{n-1} \left(b_{n,k+1}^{(\nu)} - b_{n,k}^{(\nu)}\right) \left(\phi^k, \phi^n\right) - b_{n,1}^{(\nu)} \left(\phi^0, \phi^n\right) \right] \\ &\geq \frac{1}{2\tau} \left[b_{n,n}^{(\nu)} \|\phi^n\|^2 - \sum_{k=1}^{n-1} \left(b_{n,k+1}^{(\nu)} - b_{n,k}^{(\nu)}\right) \|\phi^k\|^2 - b_{n,1}^{(\nu)} \|\phi^0\|^2 \right], \end{aligned} \quad (31)$$

where we used $\sum_{k=1}^{n-1} \left(b_{n,k+1}^{(\nu)} - b_{n,k}^{(\nu)}\right) + b_{n,1}^{(\nu)} = b_{n,n}^{(\nu)}$.

By construction,

$$2 \left(\Theta_{\phi,n}^{(\nu)} - \Theta_{\phi,n-1}^{(\nu)}\right) = b_{n,n}^{(\nu)} \|\phi^n\|^2 + \sum_{k=1}^{n-1} \left(b_{n,k}^{(\nu)} - b_{n-1,k}^{(\nu)}\right) \|\phi^k\|^2$$

and $b_{n,k}^{(\nu)} - b_{n-1,k}^{(\nu)} = -\left(b_{n,k+1}^{(\nu)} - b_{n,k}^{(\nu)}\right) + \delta_{n,k}^{(\nu)}$, therefore

$$2 \left(\Theta_{\phi,n}^{(\nu)} - \Theta_{\phi,n-1}^{(\nu)}\right) = b_{n,n}^{(\nu)} \|\phi^n\|^2 - \sum_{k=1}^{n-1} \left(b_{n,k+1}^{(\nu)} - b_{n,k}^{(\nu)}\right) \|\phi^k\|^2 + \sum_{k=1}^{n-1} \delta_{n,k}^{(\nu)} \|\phi^k\|^2. \quad (32)$$

Using (32), we conclude from (31) that

$$\left(\Delta_\tau^{\nu(t_n)}\phi^n, \phi^n\right) \geq \frac{1}{\tau} \left(\Theta_{\phi,n}^{(\nu)} - \Theta_{\phi,n-1}^{(\nu)}\right) - \frac{1}{2\tau} \sum_{k=1}^{n-1} \delta_{n,k}^{(\nu)} \|\phi^k\|^2 - \frac{1}{2\tau} b_{n,1}^{(\nu)} \|\phi^0\|^2.$$

Since $-\delta_{n,k}^{(\nu)} \geq -\left(\delta_{n,k}^{(\nu)}\right)_+$, we have

$$\left(\Delta_\tau^{\nu(t_n)}\phi^n, \phi^n\right) \geq \frac{1}{\tau} \left(\Theta_{\phi,n}^{(\nu)} - \Theta_{\phi,n-1}^{(\nu)}\right) - \frac{1}{2\tau} \sum_{k=1}^{n-1} \left(\delta_{n,k}^{(\nu)}\right)_+ \|\phi^k\|^2 - \frac{1}{2\tau} b_{n,1}^{(\nu)} \|\phi^0\|^2. \quad (33)$$

By definition of $R_{\phi,n}^{(\nu)}$, we have

$$R_{\phi,n}^{(\nu)} - R_{\phi,n-1}^{(\nu)} = \frac{1}{2} \sum_{k=1}^{n-1} \left(\delta_{n,k}^{(\nu)}\right)_+ \|\phi^k\|^2. \quad (34)$$

Therefore, combining (33), (34) and (29), we immediately arrive at the assertion of the lemma. \square

Lemma 2.8. *Given the sequence $\{\phi^n\}$, $\phi^n \in L^2(\Omega)$, the following inequality holds:*

$$\left(\Delta_\tau^{\nu(t_n)}\phi^n, \phi^n\right) \geq \frac{1}{2} \Delta_\tau^{\nu(t_n)} \|\phi^n\|^2.$$

Proof. This inequality immediately follows from the definition in (15), the Cauchy inequality, and Young's inequality. \square

For the convergence analysis, we use the abstract discrete fractional Grönwall lemma of [28]. Its application to the present variable-order L1 discretization requires verification of assumptions A1–A3 for the associated discrete kernels. For convenience, Appendix A recalls these assumptions, the complementary kernels, and the version of the discrete Grönwall theorem used here. It is shown there that the kernels generated by $\Delta_\tau^{\nu(t_n)}$ satisfy assumptions A1–A3 with comparison exponent $\nu_* = \min_{t \in [0, T]} \nu(t)$.

Lemma 2.9. *Assume that there exist constants $0 < \nu_* < \nu^* < 1$ such that $\nu(t) \in [\nu_*, \nu^*]$ for all $t \in [0, T]$. For $1 \leq k \leq n \leq N$, set $\nu_n = \nu(t_n)$, $t_n \in \mathcal{I}_N$, and define*

$$A_{n-k}^{(n)} = \frac{1}{\tau} b_{n,k}^{(\nu)},$$

or, equivalently,

$$A_{n-k}^{(n)} = \frac{1}{\tau} \int_{t_{k-1}}^{t_k} \omega_{1-\nu_n}(t_n - s) ds, \quad \omega_{1-\nu}(t) = \frac{t^{-\nu}}{\Gamma(1-\nu)}.$$

Then the kernels $\{A_{n-k}^{(n)}\}$ satisfy Assumptions A1–A3 of [28], where the fixed exponent appearing in A2 is chosen as ν_* , and

$$\rho = 1, \quad \pi_A = \frac{\Gamma(1-\nu^*)}{\Gamma(1-\nu_*)} \max\{1, T^{\nu^*-\nu_*}\}.$$

Proof. For each fixed n , the function $f(x) = \omega_{1-\nu_n}(x)$ is positive and strictly decreasing on $(0, \infty)$. Therefore, the function $g(s) = f(t_n - s)$ is positive and strictly increasing on $[0, t_n]$. Since the mesh is uniform, for $k = 1, \dots, n-1$,

$$\int_{t_{k-1}}^{t_k} g(s) ds \leq \int_{t_k}^{t_{k+1}} g(s) ds.$$

Therefore,

$$A_{n-k}^{(n)} \leq A_{n-k-1}^{(n)}, \quad k = 1, \dots, n-1,$$

or, equivalently,

$$A_0^{(n)} \geq A_1^{(n)} \geq \dots \geq A_{n-1}^{(n)} > 0.$$

Thus A1 holds.

Next, let $x \in (0, T]$. Since $\nu_n \in [\nu_*, \nu^*]$, we have

$$\omega_{1-\nu_n}(x) = \frac{\Gamma(1-\nu_*)}{\Gamma(1-\nu_n)} x^{-(\nu_n-\nu_*)} \omega_{1-\nu_*}(x).$$

Because Γ is decreasing on $(0, 1)$ and $1-\nu_n \geq 1-\nu^*$, it follows that $\Gamma(1-\nu_n) \leq \Gamma(1-\nu^*)$, and hence

$$\frac{\Gamma(1-\nu_*)}{\Gamma(1-\nu_n)} \geq \frac{\Gamma(1-\nu_*)}{\Gamma(1-\nu^*)}.$$

Moreover, since $0 \leq \nu_n - \nu_* \leq \nu^* - \nu_*$ and $0 < x \leq T$,

$$x^{-(\nu_n-\nu_*)} \geq \frac{1}{\max\{1, T^{\nu^*-\nu_*}\}}.$$

Therefore

$$\omega_{1-\nu_n}(x) \geq \frac{\Gamma(1-\nu_*)}{\Gamma(1-\nu^*) \max\{1, T^{\nu^*-\nu_*}\}} \omega_{1-\nu_*}(x) = \frac{1}{\pi_A} \omega_{1-\nu_*}(x).$$

Applying this estimate with $x = t_n - s$, for a.e. $s \in (t_{k-1}, t_k)$, and integrating over (t_{k-1}, t_k) gives

$$A_{n-k}^{(n)} \geq \frac{1}{\pi_{AT}} \int_{t_{k-1}}^{t_k} \omega_{1-\nu_*}(t_n - s) ds, \quad 1 \leq k \leq n \leq N.$$

Thus A2 holds with the fixed exponent ν_* .

Finally, since the mesh is uniform, $\rho_k = \frac{\tau_k}{\tau_{k+1}} = 1$, so A3 holds with $\rho = 1$. \square

We now present the stability result.

Theorem 2.10 (Stability). *Let $(\mathbf{u}_h^n, p_h^n, \mathbf{B}_h^n) \in \mathcal{V}_h \times \mathcal{Q}_h \times \mathcal{C}_h$ be the solution of Problem 2.3. Suppose Assumptions 2.4 and 2.5 hold, and let $\mathcal{E}_{\mathbf{u},n}^{(\alpha)}$ and $\mathcal{E}_{\mathbf{B},n}^{(\beta)}$ be defined as in Lemma 2.7. Then the fully discrete solution satisfies*

$$\begin{aligned} & \mathcal{E}_{\mathbf{u},n}^{(\alpha)} + \mathcal{E}_{\mathbf{B},n}^{(\beta)} + \frac{\tau}{2} \sum_{k=1}^n \left(\frac{1}{\text{Re}} \|\nabla \mathbf{u}_h^k\|^2 + \frac{1}{\text{Rm}} \|\nabla \mathbf{B}_h^k\|^2 + \zeta \|\nabla \cdot \mathbf{u}_h^k\|^2 + \chi \|\nabla \cdot \mathbf{B}_h^k\|^2 \right) \\ & \leq C (\|\mathbf{u}_h^0\|^2 + \|\mathbf{B}_h^0\|^2) + C\tau \sum_{k=1}^n \left(\|\mathbf{f}^k\|_{H^{-1}}^2 + \|\mathbf{g}^k\|_{H^{-1}}^2 \right) \end{aligned}$$

for all $1 \leq n \leq N$, where $C > 0$ is independent of h and τ .

Proof. Choose $(\mathbf{v}_h, q_h, \mathbf{C}_h) = (\mathbf{u}_h^n, p_h^n, \mathbf{B}_h^n)$ in (20)–(22), then sum the resulting identities, and use (10) to obtain

$$\begin{aligned} & \left(\Delta_\tau^{\alpha(t_n)} \mathbf{u}_h^n, \mathbf{u}_h^n \right) + \left(\Delta_\tau^{\beta(t_n)} \mathbf{B}_h^n, \mathbf{B}_h^n \right) + \frac{1}{\text{Re}} \|\nabla \mathbf{u}_h^n\|^2 + \frac{1}{\text{Rm}} \|\nabla \mathbf{B}_h^n\|^2 \\ & + \zeta \|\nabla \cdot \mathbf{u}_h^n\|^2 + \chi \|\nabla \cdot \mathbf{B}_h^n\|^2 = \langle \mathbf{f}^n, \mathbf{u}_h^n \rangle + \langle \mathbf{g}^n, \mathbf{B}_h^n \rangle. \end{aligned} \quad (35)$$

Applying Lemma 2.7, we obtain

$$\begin{aligned} \left(\Delta_{\tau}^{\alpha(t_n)} \mathbf{u}_h^n, \mathbf{u}_h^n \right) &\geq \frac{1}{\tau} \left(\mathcal{E}_{\mathbf{u},n}^{(\alpha)} - \mathcal{E}_{\mathbf{u},n-1}^{(\alpha)} \right) - \frac{1}{2\tau} b_{n,1}^{(\alpha)} \|\mathbf{u}_h^0\|^2, \\ \left(\Delta_{\tau}^{\beta(t_n)} \mathbf{B}_h^n, \mathbf{B}_h^n \right) &\geq \frac{1}{\tau} \left(\mathcal{E}_{\mathbf{B},n}^{(\beta)} - \mathcal{E}_{\mathbf{B},n-1}^{(\beta)} \right) - \frac{1}{2\tau} b_{n,1}^{(\beta)} \|\mathbf{B}_h^0\|^2. \end{aligned}$$

The terms in the right-hand side are estimated as follows:

$$|\langle \mathbf{f}^n, \mathbf{u}_h^n \rangle| + |\langle \mathbf{g}^n, \mathbf{B}_h^n \rangle| \leq \frac{1}{2\text{Re}} \|\nabla \mathbf{u}_h^n\|^2 + \frac{1}{2\text{Rm}} \|\nabla \mathbf{B}_h^n\|^2 + C \left(\|\mathbf{f}^n\|_{H^{-1}}^2 + \|\mathbf{g}^n\|_{H^{-1}}^2 \right).$$

Using the estimates derived above in (35), then summing the resulting inequalities over n , we obtain

$$\begin{aligned} &\mathcal{E}_{\mathbf{u},n}^{(\alpha)} + \mathcal{E}_{\mathbf{B},n}^{(\beta)} + \frac{\tau}{2\text{Re}} \sum_{k=1}^n \|\nabla \mathbf{u}_h^k\|^2 + \frac{\tau}{2\text{Rm}} \sum_{k=1}^n \|\nabla \mathbf{B}_h^k\|^2 + \zeta\tau \sum_{k=1}^n \|\nabla \cdot \mathbf{u}_h^k\|^2 + \chi\tau \sum_{k=1}^n \|\nabla \cdot \mathbf{B}_h^k\|^2 \\ &\leq \mathcal{E}_{\mathbf{u},0}^{(\alpha)} + \mathcal{E}_{\mathbf{B},0}^{(\beta)} + \frac{1}{2} \left(\sum_{k=1}^n b_{k,1}^{(\alpha)} \right) \|\mathbf{u}_h^0\|^2 + \frac{1}{2} \left(\sum_{k=1}^n b_{k,1}^{(\beta)} \right) \|\mathbf{B}_h^0\|^2 + C\tau \sum_{k=1}^n \left(\|\mathbf{f}^k\|_{H^{-1}}^2 + \|\mathbf{g}^k\|_{H^{-1}}^2 \right). \end{aligned} \quad (36)$$

Finally, taking into account (25), and $\mathcal{E}_{\mathbf{u},0}^{(\alpha)} = 0$, $\mathcal{E}_{\mathbf{B},0}^{(\beta)} = 0$, we arrive at the assertion of the theorem. \square

We employ the Stokes projector $(\Pi_h \mathbf{u}^n, \Psi_h p^n) \in \mathcal{V}_h \times \mathcal{Q}_h$ defined as

$$\begin{aligned} (\nabla (\Pi_h \mathbf{u}^n - \mathbf{u}^n), \nabla \mathbf{v}_h) - (\Psi_h p^n - p^n, \nabla \cdot \mathbf{v}_h) &= 0, \\ (\nabla \cdot (\Pi_h \mathbf{u}^n - \mathbf{u}^n), q_h) &= 0 \end{aligned}$$

for all $\mathbf{v}_h \in \mathcal{V}_h$, $q_h \in \mathcal{Q}_h$, and an elliptic projector Ξ_h defined as

$$(\nabla (\Xi_h \mathbf{B}^n - \mathbf{B}^n), \nabla \mathbf{C}_h) = 0$$

for all $\mathbf{C}_h \in \mathcal{C}_h$. Further, we introduce the decomposition

$$\begin{aligned} \mathbf{u}^n - \mathbf{u}_h^n &= (\mathbf{u}^n - \Pi_h \mathbf{u}^n) + (\Pi_h \mathbf{u}^n - \mathbf{u}_h^n) = \psi_{\mathbf{u}}^n + \xi_{\mathbf{u}}^n, \\ p^n - p_h^n &= (p^n - \Psi_h p^n) + (\Psi_h p^n - p_h^n) = \psi_p^n + \xi_p^n, \\ \mathbf{B}^n - \mathbf{B}_h^n &= (\mathbf{B}^n - \Xi_h \mathbf{B}^n) + (\Xi_h \mathbf{B}^n - \mathbf{B}_h^n) = \psi_{\mathbf{B}}^n + \xi_{\mathbf{B}}^n. \end{aligned} \quad (37)$$

By the approximation properties of Π_h and Ξ_h , we have

$$\|\psi_{\mathbf{u}}^n\| + h \|\nabla \psi_{\mathbf{u}}^n\| \leq Ch^{l+1} \|\mathbf{u}^n\|_{H^{l+1}}, \quad \|\psi_{\mathbf{B}}^n\| + h \|\nabla \psi_{\mathbf{B}}^n\| \leq Ch^{m+1} \|\mathbf{B}^n\|_{H^{m+1}} \quad (38)$$

for $0 \leq n \leq N$.

Now we discuss the convergence of the proposed method. To simplify the presentation, we will limit ourselves to the case $\alpha(t) = \beta(t)$.

Theorem 2.11 (Convergence). *Let $(\mathbf{u}_h^n, p_h^n, \mathbf{B}_h^n) \in \mathcal{V}_h \times \mathcal{Q}_h \times \mathcal{C}_h$ be the solution of Problem 2.3. Assume that $\alpha(t) = \beta(t)$ on $[0, T]$, and that $\|\Pi_h \mathbf{u}^0 - \mathbf{u}_h^0\| \leq Ch^l$ and $\|\Xi_h \mathbf{B}^0 - \mathbf{B}_h^0\| \leq Ch^m$, where l and m are defined in (38). Under Assumptions 2.4 and 2.5, there exists $\tau_0 > 0$, independent of h , such that for $0 < h \leq 1$ and $0 < \tau \leq \tau_0$,*

$$\|\mathbf{u}(t_n) - \mathbf{u}_h^n\| + \|\mathbf{B}(t_n) - \mathbf{B}_h^n\| \leq C \left(h^{\min\{l,m\}} + \tau \right), \quad 1 \leq n \leq N,$$

where C is independent of h and τ .

Proof. Denote $E_n = \|\xi_{\mathbf{u}}^n\|^2 + \|\xi_{\mathbf{B}}^n\|^2$, $D_n = \|\nabla \xi_{\mathbf{u}}^n\|^2 + \|\nabla \xi_{\mathbf{B}}^n\|^2$. Subtract the identities (20)–(22) from the identities (17)–(19), use the decomposition (37), then choose $(\mathbf{v}_h, q_h, \mathbf{C}_h) = (\xi_{\mathbf{u}}^n, \xi_p^n, \xi_{\mathbf{B}}^n)$ to obtain

$$\begin{aligned}
& \left(\Delta_{\tau}^{\alpha(t_n)} \xi_{\mathbf{u}}^n, \xi_{\mathbf{u}}^n \right) + \left(\Delta_{\tau}^{\alpha(t_n)} \xi_{\mathbf{B}}^n, \xi_{\mathbf{B}}^n \right) + \left(\Delta_{\tau}^{\alpha(t_n)} \psi_{\mathbf{u}}^n, \xi_{\mathbf{u}}^n \right) \\
& + \left(\Delta_{\tau}^{\alpha(t_n)} \psi_{\mathbf{B}}^n, \xi_{\mathbf{B}}^n \right) + \frac{1}{\text{Re}} \|\nabla \xi_{\mathbf{u}}^n\|^2 + \frac{1}{\text{Rm}} \|\nabla \xi_{\mathbf{B}}^n\|^2 \\
& + \ell(\xi_{\mathbf{u}}^n; \mathbf{u}^n, \xi_{\mathbf{u}}^n) + \ell(\psi_{\mathbf{u}}^n; \mathbf{u}^n, \xi_{\mathbf{u}}^n) + \ell(\mathbf{u}_h^n; \psi_{\mathbf{u}}^n, \xi_{\mathbf{u}}^n) \\
& + \ell(\xi_{\mathbf{B}}^n; \mathbf{B}^n, \xi_{\mathbf{B}}^n) + \ell(\psi_{\mathbf{B}}^n; \mathbf{B}^n, \xi_{\mathbf{B}}^n) + \ell(\mathbf{u}_h^n; \psi_{\mathbf{B}}^n, \xi_{\mathbf{B}}^n) \\
& - \ell(\xi_{\mathbf{B}}^n; \mathbf{B}^n, \xi_{\mathbf{u}}^n) - \ell(\psi_{\mathbf{B}}^n; \mathbf{B}^n, \xi_{\mathbf{u}}^n) - \ell(\mathbf{B}_h^n; \psi_{\mathbf{B}}^n, \xi_{\mathbf{u}}^n) \\
& - \ell(\xi_{\mathbf{B}}^n; \mathbf{u}^n, \xi_{\mathbf{B}}^n) - \ell(\psi_{\mathbf{B}}^n; \mathbf{u}^n, \xi_{\mathbf{B}}^n) - \ell(\mathbf{B}_h^n; \psi_{\mathbf{u}}^n, \xi_{\mathbf{B}}^n) \\
& + \chi \|\nabla \cdot \xi_{\mathbf{B}}^n\|^2 + \zeta \|\nabla \cdot \xi_{\mathbf{u}}^n\|^2 + \chi (\nabla \cdot \psi_{\mathbf{B}}^n, \nabla \cdot \xi_{\mathbf{B}}^n) \\
& + \zeta (\nabla \cdot \psi_{\mathbf{u}}^n, \nabla \cdot \xi_{\mathbf{u}}^n) + (\mathbf{r}_1^n, \xi_{\mathbf{u}}^n) + (\mathbf{r}_2^n, \xi_{\mathbf{B}}^n) = 0.
\end{aligned} \tag{39}$$

Using Lemma 2.7, we have:

$$\left(\Delta_{\tau}^{\alpha(t_n)} \xi_{\mathbf{u}}^n, \xi_{\mathbf{u}}^n \right) + \left(\Delta_{\tau}^{\alpha(t_n)} \xi_{\mathbf{B}}^n, \xi_{\mathbf{B}}^n \right) \geq \frac{1}{2} \Delta_{\tau}^{\alpha(t_n)} E_n.$$

Next,

$$\left| \left(\Delta_{\tau}^{\alpha(t_n)} \psi_{\mathbf{u}}^n, \xi_{\mathbf{u}}^n \right) \right| \leq \frac{\epsilon}{\text{Re}} \|\nabla \xi_{\mathbf{u}}^n\|^2 + C_{\epsilon} \text{Re} \|\Delta_{\tau}^{\alpha(t_n)} \psi_{\mathbf{u}}^n\|^2.$$

Further, using the relation $\psi_{\mathbf{u}}^k - \psi_{\mathbf{u}}^{k-1} = (\mathbf{u}^k - \mathbf{u}^{k-1}) - \Pi_h(\mathbf{u}^k - \mathbf{u}^{k-1})$, and the approximation property of Π_h , we obtain

$$\|\psi_{\mathbf{u}}^k - \psi_{\mathbf{u}}^{k-1}\| \leq C_{\tau} h^{l+1} \sup_{t \in [t_{k-1}, t_k]} \|\partial_t \mathbf{u}(t)\|_{H^{l+1}}.$$

Hence, by using (15), (24) and (38), we have

$$\begin{aligned}
\|\Delta_{\tau}^{\alpha(t_n)} \psi_{\mathbf{u}}^n\| & \leq \frac{1}{\tau} \sum_{k=1}^n b_{n,k}^{(\alpha)} \|\psi_{\mathbf{u}}^k - \psi_{\mathbf{u}}^{k-1}\| \\
& \leq C h^{l+1} \left(\sum_{k=1}^n b_{n,k}^{(\alpha)} \right) \sup_{t \in [0, t_n]} \|\partial_t \mathbf{u}(t)\|_{H^{l+1}} \leq C h^{l+1} \sup_{t \in [0, T]} \|\partial_t \mathbf{u}(t)\|_{H^{l+1}}.
\end{aligned}$$

Therefore, for any $\epsilon > 0$,

$$\left| \left(\Delta_{\tau}^{\alpha(t_n)} \psi_{\mathbf{u}}^n, \xi_{\mathbf{u}}^n \right) \right| \leq \frac{\epsilon}{\text{Re}} \|\nabla \xi_{\mathbf{u}}^n\|^2 + C_{\epsilon} h^{2l+2} \sup_{t \in [0, T]} \|\partial_t \mathbf{u}(t)\|_{H^{l+1}}^2.$$

Similarly,

$$\left| \left(\Delta_{\tau}^{\alpha(t_n)} \psi_{\mathbf{B}}^n, \xi_{\mathbf{B}}^n \right) \right| \leq \frac{\epsilon}{\text{Rm}} \|\nabla \xi_{\mathbf{B}}^n\|^2 + C_{\epsilon} h^{2m+2} \sup_{t \in [0, T]} \|\partial_t \mathbf{B}(t)\|_{H^{m+1}}^2.$$

We now estimate the nonlinear terms. By Hölder's inequality, the two-dimensional Ladyzhenskaya inequality, the Poincaré inequality, and Young's inequality, we obtain for any $\epsilon > 0$:

$$\begin{aligned}
|\ell(\xi_{\mathbf{u}}^n; \mathbf{u}^n, \xi_{\mathbf{u}}^n)| & \leq \frac{\epsilon}{\text{Re}} \|\nabla \xi_{\mathbf{u}}^n\|^2 + C_{\epsilon} \|\xi_{\mathbf{u}}^n\|^2 \|\mathbf{u}^n\|_{W^{1,\infty}}^2, \\
|\ell(\psi_{\mathbf{u}}^n; \mathbf{u}^n, \xi_{\mathbf{u}}^n)| & \leq \frac{\epsilon}{\text{Re}} \|\nabla \xi_{\mathbf{u}}^n\|^2 + C_{\epsilon} \|\nabla \psi_{\mathbf{u}}^n\|^2 \|\mathbf{u}^n\|_{H^1}^2.
\end{aligned}$$

The other nonlinear terms of the same form are estimated analogously.

Using the error decomposition (37) and the trilinearity of ℓ , we decompose the term involving the discrete solution into contributions of the exact solution, the projection error, and the discrete error:

$$|\ell(\mathbf{u}_h^n; \psi_{\mathbf{u}}^n, \xi_{\mathbf{u}}^n)| \leq |\ell(\mathbf{u}^n; \psi_{\mathbf{u}}^n, \xi_{\mathbf{u}}^n)| + |\ell(\psi_{\mathbf{u}}^n; \psi_{\mathbf{u}}^n, \xi_{\mathbf{u}}^n)| + |\ell(\xi_{\mathbf{u}}^n; \psi_{\mathbf{u}}^n, \xi_{\mathbf{u}}^n)|.$$

Applying Hölder's inequality, the two-dimensional Ladyzhenskaya inequality, the Poincaré inequality, the inverse inequality for finite element functions, and Young's inequality, we obtain

$$|\ell(\mathbf{u}_h^n; \psi_{\mathbf{u}}^n, \xi_{\mathbf{u}}^n)| \leq \frac{\epsilon}{\text{Re}} \|\nabla \xi_{\mathbf{u}}^n\|^2 + C_{\epsilon} \|\mathbf{u}^n\|_{L^{\infty}}^2 \|\psi_{\mathbf{u}}^n\|^2 + C_{\epsilon} \|\nabla \psi_{\mathbf{u}}^n\|^4 + Ch^{-1} \|\nabla \psi_{\mathbf{u}}^n\|^2 \|\xi_{\mathbf{u}}^n\|^2.$$

The corresponding terms involving \mathbf{B}_h^n are handled analogously and are omitted for brevity.

The rest of the terms are estimated as follows:

$$\chi |(\nabla \cdot \psi_{\mathbf{B}}^n, \nabla \cdot \xi_{\mathbf{B}}^n)| + \zeta |(\nabla \cdot \psi_{\mathbf{u}}^n, \nabla \cdot \xi_{\mathbf{u}}^n)| \leq \frac{\chi}{2} \|\nabla \cdot \xi_{\mathbf{B}}^n\|^2 + \frac{\zeta}{2} \|\nabla \cdot \xi_{\mathbf{u}}^n\|^2 + C (\|\nabla \psi_{\mathbf{B}}^n\|^2 + \|\nabla \psi_{\mathbf{u}}^n\|^2),$$

$$|(\mathbf{r}_1^n, \xi_{\mathbf{u}}^n)| + |(\mathbf{r}_2^n, \xi_{\mathbf{B}}^n)| \leq \frac{\epsilon}{\text{Re}} \|\nabla \xi_{\mathbf{u}}^n\|^2 + \frac{\epsilon}{\text{Rm}} \|\nabla \xi_{\mathbf{B}}^n\|^2 + C (\|\mathbf{r}_1^n\|^2 + \|\mathbf{r}_2^n\|^2).$$

Using the estimates derived above in (39), and choosing $\epsilon > 0$ sufficiently small, we collect all terms involving $\|\nabla \xi_{\mathbf{u}}^n\|^2$ and $\|\nabla \xi_{\mathbf{B}}^n\|^2$ on the left-hand side to obtain

$$\frac{1}{2} \Delta_{\tau}^{\alpha(t_n)} E_n + c_0 D_n + \frac{\chi}{2} \|\nabla \cdot \xi_{\mathbf{B}}^n\|^2 + \frac{\zeta}{2} \|\nabla \cdot \xi_{\mathbf{u}}^n\|^2 \leq I_1 + I_2,$$

where $c_0 = \frac{1}{2} \min \left\{ \frac{1}{\text{Re}}, \frac{1}{\text{Rm}} \right\}$, and

$$\begin{aligned} I_1 &= C (1 + h^{-1} \|\nabla \psi_{\mathbf{u}}^n\|^2 + h^{-1} \|\nabla \psi_{\mathbf{B}}^n\|^2) (\|\xi_{\mathbf{u}}^n\|^2 + \|\xi_{\mathbf{B}}^n\|^2), \\ I_2 &= C (\|\nabla \psi_{\mathbf{u}}^n\|^2 + \|\nabla \psi_{\mathbf{B}}^n\|^2 + \|\nabla \psi_{\mathbf{u}}^n\|^4 + \|\nabla \psi_{\mathbf{B}}^n\|^4 + \tau^2). \end{aligned}$$

Next, invoking the projection estimates (38), we infer that

$$I_1 + I_2 \leq C_1 E_n + C (h^{2l} + h^{2m} + \tau^2)$$

for $0 < h \leq 1$, where C_1 is independent of h , τ and n . Therefore,

$$\frac{1}{2} \Delta_{\tau}^{\alpha(t_n)} E_n + c_0 D_n \leq C_1 E_n + R, \quad (40)$$

where $R = C (h^{2l} + h^{2m} + \tau^2)$.

Using the definition of the coefficients $b_{n,k}^{(\alpha)}$, one checks directly that

$$\Delta_{\tau}^{\alpha(t_n)} E_n = \sum_{k=1}^n A_{n-k}^{(n)} \nabla_{\tau} E_k, \quad A_{n-k}^{(n)} = \frac{1}{\tau} b_{n,k}^{(\alpha)}, \quad \nabla_{\tau} E_k = E_k - E_{k-1}.$$

Hence it follows from (40) that

$$\sum_{k=1}^n A_{n-k}^{(n)} \nabla_{\tau} E_k \leq 2C_1 E_n + 2R. \quad (41)$$

By setting $v^n = E_n$, $\theta = 0$, $g^n = 2R$, and choosing $\lambda_0 = 2C_1$, $\lambda_s = 0$, $1 \leq s \leq N-1$, Eq. (41) can be written as

$$\sum_{k=1}^n A_{n-k}^{(n)} \nabla_{\tau} v^k \leq \sum_{k=1}^n \lambda_{n-k} v^k + g^n, \quad 1 \leq n \leq N.$$

Thus (41) has the form required by Theorem 3.2 of [28] (see Appendix A) with

$$\Lambda \geq \sum_{s=0}^{N-1} \lambda_s = 2C_1.$$

Taking $\Lambda = 2C_1$, and using Lemma 2.9, Assumptions A1–A3 in [28] hold with exponent α_* , constant π_A , and $\rho = 1$. Therefore the step-size condition in Theorem 3.2 of [28] becomes

$$\tau \leq (2\pi_A \Gamma(2 - \alpha_*) \Lambda)^{-1/\alpha_*} = (4\pi_A \Gamma(2 - \alpha_*) C_1)^{-1/\alpha_*},$$

and Theorem 3.2 gives

$$E_n \leq 2\mathbb{E}_{\alpha_*}(4\pi_A C_1 t_n^{\alpha_*}) \left(E_0 + \max_{1 \leq k \leq n} \sum_{j=1}^k 2\mathcal{P}_{k-j}^{(k)} R \right),$$

where \mathbb{E}_{α_*} is the Mittag–Leffler function and, for each $1 \leq z \leq N$, $\left\{ \mathcal{P}_{z-j}^{(z)} \right\}_{j=1}^z$ are the complementary kernels associated with the discrete kernels $\left\{ A_{z-k}^{(z)} \right\}_{k=1}^z$. By Remark 1 following Theorem 3.1 in [28], we have for $1 \leq k \leq n$,

$$\sum_{j=1}^k 2\mathcal{P}_{k-j}^{(k)} R \leq 2\pi_A \Gamma(1 - \alpha_*) T^{\alpha_*} R.$$

Consequently,

$$E_n \leq 2\mathbb{E}_{\alpha_*}(4\pi_A C_1 t_n^{\alpha_*}) (E_0 + 2\pi_A \Gamma(1 - \alpha_*) T^{\alpha_*} R).$$

Therefore, using $t_n \leq T$, we obtain

$$E_n \leq C (E_0 + R), \quad 1 \leq n \leq N,$$

and considering that $E_0 \leq C (h^{2l} + h^{2m})$, we arrive at the assertion of the theorem. \square

2.4 Implementation of the Fully Discrete Scheme

For the numerical implementation, the fully implicit scheme (20)–(22) is solved at each time step by a Picard linearization initialized by the solution from the previous time step. This leads, at every Picard iteration, to a monolithic linear system [41] for the coupled velocity–pressure–magnetic-field unknowns, which is solved by restarted FGMRES with a block preconditioner.

In addition to the stabilization terms included in the discrete formulation, the numerical implementation uses a divergence-cleaning step for the magnetic field after each time step. More precisely, after solving Problem 2.3 at time level t_n , we obtain $(\mathbf{u}_h^n, p_h^n, \tilde{\mathbf{B}}_h^n)$, where $\tilde{\mathbf{B}}_h^n$ denotes the magnetic field before the cleaning step. We then solve the auxiliary elliptic problem to find $\phi_h^n \in \Psi_h$ such that

$$(\nabla \phi_h^n, \nabla \psi_h) = (\nabla \cdot \tilde{\mathbf{B}}_h^n, \psi_h), \quad (42)$$

for all $\psi_h \in \Psi_h$, where

$$\Psi_h = \left\{ \psi \in H^1(\Omega) : \int_{\Omega} \psi \, d\mathbf{x} = 0 \right\},$$

and then set

$$\mathbf{B}_h^n = \tilde{\mathbf{B}}_h^n - \nabla \phi_h^n. \quad (43)$$

In the periodic test cases, (42) is solved with periodic boundary conditions, and the zero-mean condition ensures uniqueness of ϕ_h^n . In the cases with Dirichlet boundary conditions for the magnetic field, the correction (43) does not in general preserve the prescribed boundary values. Therefore, after the cleaning step, the Dirichlet values are imposed again before proceeding to the next time level.

3 Results

This section presents a set of numerical tests to assess the correctness of the numerical scheme and the effect of variable-order fractional time derivatives on MHD flow. Although the formulation allows different variable orders in the momentum and induction equations, we set $\alpha(t) = \beta(t)$ in most of the numerical experiments to reduce the parameter space. The case $\alpha(t) \neq \beta(t)$ is studied in Section 3.3.4.

3.1 Convergence of the Numerical Scheme

The first numerical experiment is designed to verify the temporal convergence of the proposed scheme. We consider the system (5)–(7) on $\Omega = (0, 1)^2$ over the time interval $(0, T]$ with $T = 1$. We take the manufactured solution

$$\mathbf{u}(\mathbf{x}, t) = \begin{pmatrix} t^4(1-x_1)^2 x_1^2 (4x_2^3 - 6x_2^2 + 2x_2) \\ -t^4(4x_1^3 - 6x_1^2 + 2x_1)(1-x_2)^2 x_2^2 \end{pmatrix}, \quad p(\mathbf{x}, t) = 0, \quad \mathbf{x} = (x_1, x_2), \quad (44)$$

$$\mathbf{B}(\mathbf{x}, t) = \begin{pmatrix} t^3(1-x_1)^2 x_1^2 (4x_2^3 - 6x_2^2 + 2x_2) \\ -t^3(4x_1^3 - 6x_1^2 + 2x_1)(1-x_2)^2 x_2^2 \end{pmatrix} \quad (45)$$

and three representative variable-order profiles. In all three cases, the fractional orders in the velocity and induction equations are taken to be the same.

Case 1. A linearly increasing variable order

$$\alpha(t) = \beta(t) = \alpha_0 + (\alpha_1 - \alpha_0) \frac{t}{T}, \quad (\alpha_0, \alpha_1) = (0.6, 0.95), \quad t \in [0, T]$$

with homogeneous Dirichlet boundary conditions for both the velocity and the magnetic field.

Case 2. A periodically varying order

$$\alpha(t) = \beta(t) = \bar{\alpha} + A_0 \sin\left(\frac{2\pi t}{P_0}\right), \quad \bar{\alpha} = 0.75, \quad A_0 = 0.2, \quad P_0 = \frac{T}{2}$$

with periodic boundary conditions for both the velocity and the magnetic field.

Case 3. A smoothly varying order

$$\alpha(t) = \beta(t) = \alpha_0 + \frac{1}{2}(\alpha_1 - \alpha_0) \left(1 + \tanh\left(\frac{t - 0.4}{0.05}\right)\right), \quad (\alpha_0, \alpha_1) = (0.6, 0.95),$$

which models a rapid transition of the fractional order around $t \approx 0.4$, with periodic boundary conditions for both the velocity and the magnetic field.

We study temporal convergence by refining the uniform time step τ while keeping the spatial mesh $h \approx 0.003535$ fixed. The parameters in the numerical scheme are chosen as follows: $\text{Re} = \text{Rm} = 1$, $\zeta = 0.5$, $\chi = 0.125$. The error is measured in the discrete norm

$$\|\mathbf{e}\|_{L^\infty(0, T; \mathbf{L}^2(\Omega))} = \max_{0 \leq n \leq N} \|\mathbf{e}^n\|_{\mathbf{L}^2(\Omega)},$$

and the observed temporal error is computed by the standard ratio

$$r = \log_2 \frac{E(\tau)}{E(\tau/2)},$$

where $E(\tau)$ denotes the error of the solution, obtained with the time step τ , in the norm defined above.

All runs in Section 3 use the same spatial discretization: Taylor-Hood elements P_2/P_1 for the 2D velocity-pressure pair (\mathbf{u}, p) , and continuous piecewise-quadratic (P_2) elements for the magnetic field \mathbf{B} . In the computations, the Picard iteration is initialized by the solution from

the previous time level and stopped when the difference between two successive iterates becomes smaller than 10^{-10} . In the reported tests, convergence is achieved within 2–3 iterations. This is likely due to the combination of a smooth exact solution, relatively weak nonlinearity, and the use of the previous time level as the initial guess.

The results in Table 1 show that the proposed variable-order fractional MHD scheme exhibits a consistent first-order temporal convergence for both \mathbf{u} and \mathbf{B} . The measured orders stay close to one (approximately 1.01 – 1.10 for \mathbf{u} and 1.03 – 1.05 for \mathbf{B}) as τ decreases from 1/10 to 1/320. This behavior agrees well with the theoretical prediction obtained in Theorem 2.11. Similar conclusions hold for Cases 2 and 3, presented in Table 2 and Table 3, respectively: in both cases, the errors decrease consistently with time-step refinement, and the computed orders remain close to one.

We also examine the behavior of the method under spatial mesh refinement with the fixed time step $\tau = 1/1000$. In all three cases, the numerical results are consistent with the expected second-order spatial convergence: the observed orders are higher on the coarser meshes but approach the asymptotic value 2 as the mesh is refined.

Table 1: Convergence analysis for Case 1. The table reports the errors in the numerical approximations of the velocity and magnetic field for successive time-step refinements $\tau = 1/10, \dots, 1/320$, together with the corresponding experimental orders of convergence.

τ	$\ \mathbf{u} - \mathbf{u}_h\ _{L^\infty(0,T;\mathbf{L}^2(\Omega))}$	Order	$\ \mathbf{B} - \mathbf{B}_h\ _{L^\infty(0,T;\mathbf{L}^2(\Omega))}$	Order
1/10	6.5261×10^{-5}	–	3.5554×10^{-5}	–
1/20	3.2445×10^{-5}	1.01	1.7411×10^{-5}	1.03
1/40	1.5825×10^{-5}	1.04	8.4499×10^{-6}	1.04
1/80	7.6090×10^{-6}	1.06	4.0834×10^{-6}	1.05
1/160	3.6152×10^{-6}	1.07	1.9704×10^{-6}	1.05
1/320	1.6855×10^{-6}	1.10	9.5280×10^{-7}	1.05

Table 2: Convergence analysis for Case 2. The table reports the errors in the numerical approximations of the velocity and magnetic field for successive time-step refinements $\tau = 1/20, \dots, 1/320$, together with the corresponding experimental orders of convergence.

τ	$\ \mathbf{u} - \mathbf{u}_h\ _{L^\infty(0,T;\mathbf{L}^2(\Omega))}$	Order	$\ \mathbf{B} - \mathbf{B}_h\ _{L^\infty(0,T;\mathbf{L}^2(\Omega))}$	Order
1/20	1.4530×10^{-5}	–	1.1774×10^{-5}	–
1/40	7.2694×10^{-6}	1.00	5.8258×10^{-6}	1.02
1/80	3.5998×10^{-6}	1.01	2.8495×10^{-6}	1.03
1/160	1.7515×10^{-6}	1.04	1.3835×10^{-6}	1.04
1/320	8.4703×10^{-7}	1.05	6.6896×10^{-7}	1.05

Table 3: Convergence analysis for Case 3. The table reports the errors in the numerical approximations of the velocity and magnetic field for successive time-step refinements $\tau = 1/10, \dots, 1/320$, together with the corresponding experimental orders of convergence.

τ	$\ \mathbf{u} - \mathbf{u}_h\ _{L^\infty(0,T;\mathbf{L}^2(\Omega))}$	Order	$\ \mathbf{B} - \mathbf{B}_h\ _{L^\infty(0,T;\mathbf{L}^2(\Omega))}$	Order
1/10	7.6527×10^{-5}	–	4.0459×10^{-5}	–
1/20	3.8289×10^{-5}	1.00	1.9917×10^{-5}	1.02
1/40	1.8819×10^{-5}	1.02	9.7121×10^{-6}	1.04
1/80	9.1632×10^{-6}	1.04	4.7137×10^{-6}	1.04
1/160	4.4372×10^{-6}	1.05	2.2827×10^{-6}	1.05
1/320	2.1399×10^{-6}	1.05	1.1050×10^{-6}	1.05

In addition to the convergence orders, we monitor the divergence norms in these tests. Figure 1 shows the time evolution of $\|\nabla \cdot \mathbf{u}_h\|$ and $\|\nabla \cdot \mathbf{B}_h\|$ for Cases 1–3. In all cases, the velocity divergence remains small, and for the magnetic field the cleaning step reduces the divergence substantially over the whole time interval. Hence, the divergence errors remain small in the convergence tests. This behavior is consistent with the use of H^1 -conforming finite element spaces, for which the constraints $\nabla \cdot \mathbf{u} = 0$ and $\nabla \cdot \mathbf{B} = 0$ are generally not satisfied exactly at the discrete level. Accordingly, one expects small but nonzero values of $\|\nabla \cdot \mathbf{u}_h\|$ and $\|\nabla \cdot \mathbf{B}_h\|$ in the numerical solution [24, 51, 52].

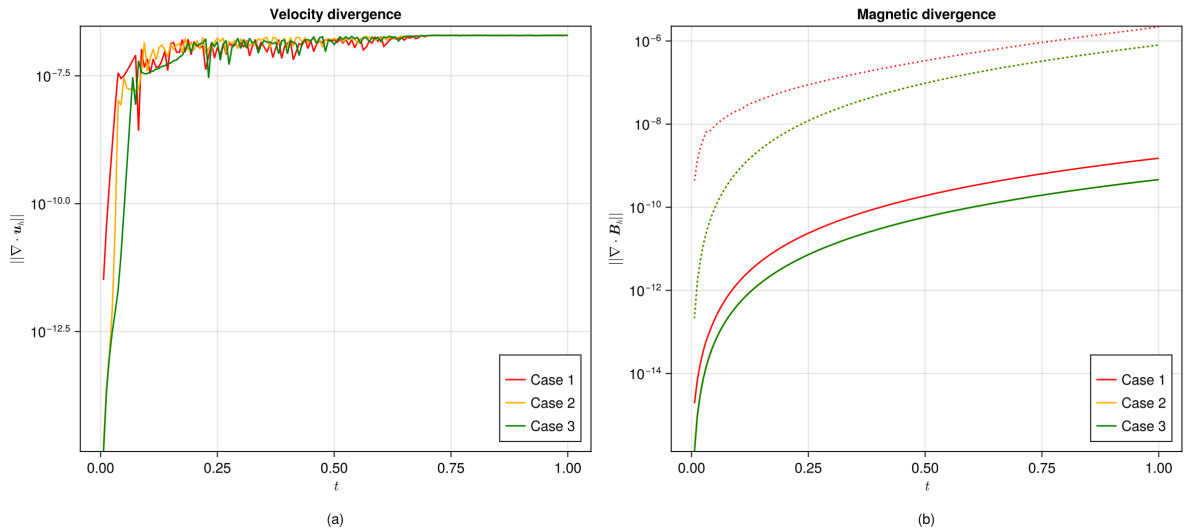


Figure 1: Time evolution of the divergence norms in the convergence tests: (a) $\|\nabla \cdot \mathbf{u}_h\|$; (b) $\|\nabla \cdot \mathbf{B}_h\|$, where the dotted and solid lines represent the values before and after the cleaning step, respectively. In panel (b), the results for Cases 2 and 3 almost coincide.

3.2 Consistency of the Variable-order Fractional MHD Model with the Classical MHD Model

The second numerical experiment verifies that the variable-order fractional MHD model under study is consistent with the classical (integer-order) MHD equations in the limit when the fractional orders $\alpha(t)$ and $\beta(t)$ approach one. To this end, we consider a one-parameter family of variable orders

$$\alpha(t) = \beta(t) = 1 - \varepsilon \left(1 - \frac{t}{T}\right) - \delta, \quad \delta = 10^{-10},$$

so that $\alpha(t), \beta(t) \in (0, 1)$ for all $t \in [0, T]$ and $\alpha(t) \rightarrow 1$ uniformly in time as $\varepsilon \rightarrow 0$. We note that the theoretical analysis is carried out under Assumption 2.5, which requires the fractional orders to be bounded away from 1. Hence, the limits $\alpha(t), \beta(t) \rightarrow 1$ are not covered by Theorem 2.11 and are examined here only numerically.

We compute solutions $(\mathbf{u}_\varepsilon, p_\varepsilon, \mathbf{B}_\varepsilon)$ on $\Omega = (0, 1)^2$ over the time interval $[0, T]$ with $T = 0.5$ starting from the initial values

$$\begin{aligned} \mathbf{u}_0(\mathbf{x}) &= \begin{pmatrix} 2\pi \sin^2(\pi x_1) \sin(\pi x_2) \cos(\pi x_2) \\ -2\pi \sin(\pi x_1) \cos(\pi x_1) \sin^2(\pi x_2) \end{pmatrix}, \\ \mathbf{B}_0(\mathbf{x}) &= \begin{pmatrix} 0.8\pi \sin^2(\pi x_1) \sin(2\pi x_2) \cos(2\pi x_2) \\ -0.4\pi \sin(\pi x_1) \cos(\pi x_1) \sin^2(2\pi x_2) \end{pmatrix} \end{aligned} \quad (46)$$

with homogeneous Dirichlet conditions for a sequence of decreasing parameters $\varepsilon \in \{0.1, 0.05, 0.03, 0.02, 0.01, 0.005, 10^{-3}, 10^{-4}, 10^{-5}, 10^{-6}\}$, and compare them against a reference integer-order solution $(\mathbf{u}_1, p_1, \mathbf{B}_1)$ obtained by setting $\alpha(t) = \beta(t) = 1$. The Reynolds numbers are

chosen as $\text{Re} = \text{Rm} = 200$, and stabilization parameters and the Picard iteration tolerance are selected as in Section 3.1. In this test, the prescribed Picard tolerance was reached within 4–6 iterations.

In this and the following tests, the classical (integer-order) incompressible MHD system is solved with the same finite element spatial discretization and the corresponding fully implicit first-order time discretization. The nonlinear systems are solved by the same Picard iteration procedure as in the fractional case.

To quantify convergence toward the integer-order model, we introduce the time-dependent errors

$$E_u^{(\varepsilon)}(t) = \|\mathbf{u}_\varepsilon(t) - \mathbf{u}_1(t)\|_{\mathbf{L}^2(\Omega)}, \quad E_B^{(\varepsilon)}(t) = \|\mathbf{B}_\varepsilon(t) - \mathbf{B}_1(t)\|_{\mathbf{L}^2(\Omega)},$$

and also examine the energy differences

$$|K_\varepsilon(t) - K_1(t)|, \quad |M_\varepsilon(t) - M_1(t)|,$$

where $K(t)$ and $M(t)$ are the kinetic and magnetic energies, respectively:

$$K(t) = \frac{1}{2} \int_{\Omega} |\mathbf{u}(\mathbf{x}, t)|^2 d\mathbf{x}, \quad M(t) = \frac{1}{2} \int_{\Omega} |\mathbf{B}(\mathbf{x}, t)|^2 d\mathbf{x}, \quad (47)$$

and subscripts ε and 1 denote a corresponding diagnostic computed from the solution obtained with a given ε and the classical MHD, respectively.

Figure 2 shows that both $E_u^{(\varepsilon)}(t)$ and $E_B^{(\varepsilon)}(t)$ decrease monotonically as ε decreases. For larger ε , the deviations from the integer-order solution grow rapidly at early times and remain noticeable over the interval shown. As ε becomes smaller, the curves are shifted downward over the whole time interval, and for $\varepsilon = 10^{-6}$ the discrepancies are reduced to the level of about 10^{-7} – 10^{-5} . This behavior is consistent with convergence of the fractional solutions to the integer-order reference as $\varepsilon \rightarrow 0$. The logarithmic insets further show the systematic reduction of the errors across several orders of magnitude.

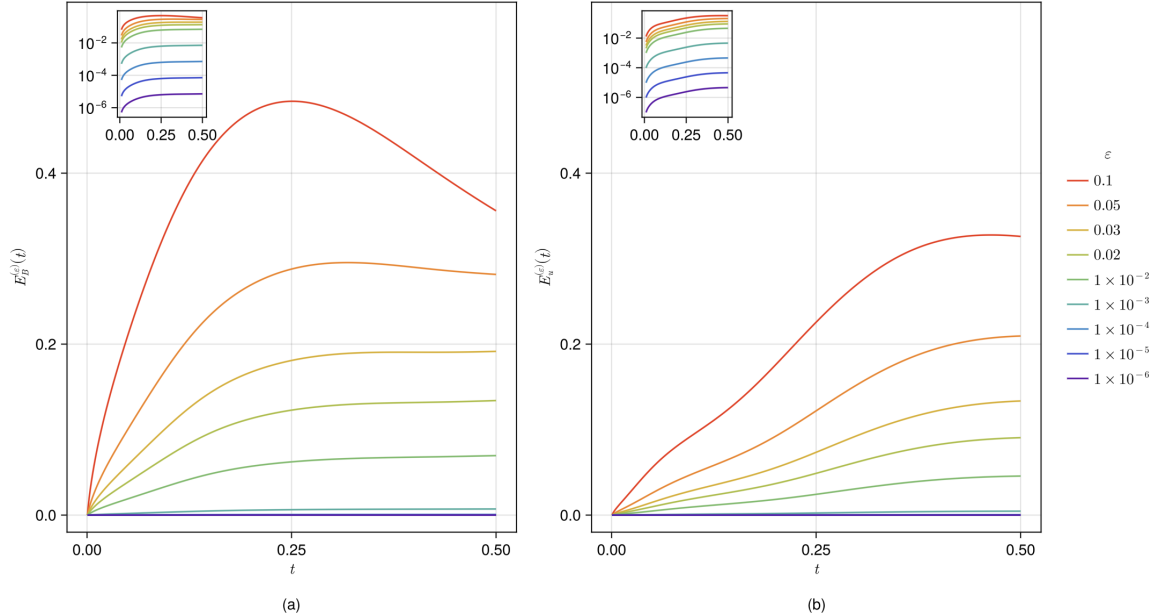


Figure 2: Time evolution of the solution discrepancies between the classical model and the fractional models defined by the variable-order law $\alpha(t) = \beta(t) = 1 - \varepsilon(1 - \frac{t}{T}) - \delta$ with $\delta = 10^{-10}$ for various ε : (a) $E_B^{(\varepsilon)}(t) = \|\mathbf{B}_\varepsilon(t) - \mathbf{B}_1(t)\|_{\mathbf{L}^2(\Omega)}$; (b) $E_u^{(\varepsilon)}(t) = \|\mathbf{u}_\varepsilon(t) - \mathbf{u}_1(t)\|_{\mathbf{L}^2(\Omega)}$. The insets show the same curves on a logarithmic scale.

Figure 3 shows the time evolution of $|K_\varepsilon(t) - K_1(t)|$ and $|M_\varepsilon(t) - M_1(t)|$. In both panels, the discrepancies decrease as ε becomes smaller. For the magnetic energy, the curves remain ordered over the whole interval, with smaller ε giving uniformly smaller values of $|M_\varepsilon(t) - M_1(t)|$. For the kinetic energy, the same overall trend is observed, although the curves pass through values close to zero near the middle of the interval. The logarithmic insets make the reduction more visible and show that the energy differences decrease by several orders of magnitude as $\varepsilon \rightarrow 0$.

These results confirm that, as $\alpha(t), \beta(t) \rightarrow 1$, the variable-order fractional MHD solutions converge to the classical MHD solution in both state variables and energies, showing that the proposed formulation and discretization correctly reproduce the classical limit.

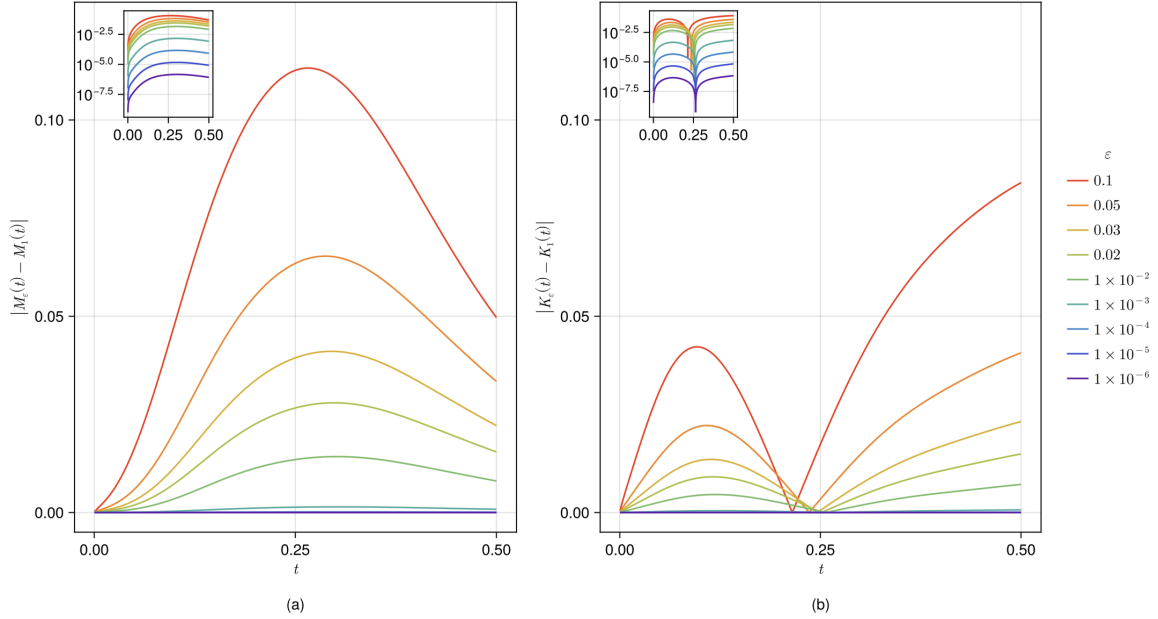


Figure 3: Time evolution of energy discrepancies between the classical model and the fractional models defined by the variable-order law $\alpha(t) = \beta(t) = 1 - \varepsilon \left(1 - \frac{t}{T}\right) - \delta$, $\delta = 10^{-10}$ for various ε : **(a)** $|M_\varepsilon(t) - M_1(t)|$; **(b)** $|K_\varepsilon(t) - K_1(t)|$. The insets show the same curves on a logarithmic scale.

3.3 Impact of the Variable-order Fractional Derivatives on the MHD Flow

In the third experiment, we study how the order of the Caputo time-fractional derivative affects the evolution of an MHD flow. We consider the fractional-order periodic divergence-free vortex test in $\Omega = (0, 1)^2$, in which the initial values are defined as

$$\mathbf{u}_0(\mathbf{x}) = \begin{pmatrix} \sin(2\pi x_1) \cos(2\pi x_2) \\ -\cos(2\pi x_1) \sin(2\pi x_2) \end{pmatrix}, \quad \mathbf{B}_0(\mathbf{x}) = \begin{pmatrix} 2 \sin(8\pi x_1) \cos(8\pi x_2) \\ -2 \cos(8\pi x_1) \sin(8\pi x_2) \end{pmatrix}, \quad (48)$$

whereas periodic boundary conditions are imposed on both velocity and magnetic field. The remaining parameters are defined as follows: $T = 0.16$, $\text{Re} = \text{Rm} = 300$, $h \approx 0.009428$, $\tau = 0.0002$. In all numerical tests presented in Section 3.3, the Picard iteration tolerance was set to 10^{-10} , and this level was reached within 3–5 iterations.

To assess both constant-order and time-dependent memory effects, we consider the following representative order functions $\alpha(t) = \beta(t)$, all satisfying $\alpha(t) \in (0, 1)$ for $t \in [0, T]$:

Case 1. Constant order:

$$\alpha(t) \equiv \alpha_c, \quad \alpha_c \in \{0.6, 0.75, 0.9\}.$$

Case 2. Linear ramp:

$$\alpha(t) = \alpha_0 + (\alpha_1 - \alpha_0) \frac{t}{T}, \quad \alpha_0 = 0.9, \quad \alpha_1 = 0.6.$$

Case 3. Step change:

$$\alpha(t) = \begin{cases} \alpha_1, & t < t_s, \\ \alpha_2, & t \geq t_s, \end{cases} \quad \alpha_1 = 0.9, \quad \alpha_2 = 0.65, \quad t_s = \frac{T}{2}.$$

Case 4. Periodic modulation (sinusoidal profile):

$$\alpha(t) = \bar{\alpha} + A_0 \sin\left(\frac{2\pi t}{P_0}\right), \quad \bar{\alpha} = 0.75, \quad A_0 = 0.15, \quad P_0 = \frac{T}{2}.$$

Case 5. Smooth step:

$$\alpha(t) = \alpha_0 + \frac{1}{2}(\alpha_1 - \alpha_0) \left(1 + \tanh\left(\frac{t - t_s}{\varepsilon}\right)\right), \quad \alpha_0 = 0.8, \quad \alpha_1 = 0.5, \quad t_s = \frac{2T}{5}, \quad \varepsilon = 0.05.$$

Here we include one case with a step-type order profile (Case 3) in order to examine the practical robustness of the numerical method in the presence of an abrupt change of memory intensity. This example lies outside the assumptions of the analysis and is therefore presented as an empirical robustness test rather than as a verification of the theoretical results.

All fractional and variable-order cases are compared against the classical MHD model obtained for $\alpha(t) \equiv 1$, $\beta(t) \equiv 1$. For each case, we monitor the kinetic energy $K(t)$ and magnetic energy $M(t)$, defined in (47), as well as the enstrophy $Z(t)$ and current enstrophy $J(t)$, given by

$$Z(t) = \frac{1}{2} \int_{\Omega} |\nabla \times \mathbf{u}(\mathbf{x}, t)|^2 d\mathbf{x} \quad \text{and} \quad J(t) = \frac{1}{2} \int_{\Omega} |\nabla \times \mathbf{B}(\mathbf{x}, t)|^2 d\mathbf{x}. \quad (49)$$

3.3.1 Choosing Stabilization Parameters

Before analyzing the influence of the variable-order profiles on the computed MHD dynamics, we first specify the stabilization parameters, the grad-div parameter ζ and the magnetic divergence-penalty parameter χ , used in the simulations. To choose suitable values, we perform a sensitivity study for the linear ramp profile (Case 2), which is taken here as a representative case.

Figure 4 shows the time evolution of the divergence norms in this study. In panel (a), the parameter χ is fixed at $\chi = 1$, and we examine the effect of ζ on $\|\nabla \cdot \mathbf{u}_h\|$. As ζ increases, the values of $\|\nabla \cdot \mathbf{u}_h\|$ decrease over the whole time interval. This decrease is clearly visible up to $\zeta = 2000$, whereas larger values only slightly modify the curves. We therefore fix $\zeta = 2000$ and then examine the role of χ . Panel (b) shows that increasing χ leads to smaller values of $\|\nabla \cdot \mathbf{B}_h\|$ throughout the simulation. The reduction is pronounced up to $\chi = 500$ and continues for larger values, although less strongly. In view of this behavior, we choose $\zeta = 2000$ and $\chi = 500$ for the computations in Section 3.3, since these values already provide a substantial reduction of both divergence norms.

To check that this choice does not materially affect the computed dynamics, we compare the kinetic energy K , magnetic energy M , enstrophy Z , and current enstrophy J for the tested parameter values. Taking the run with $(\zeta, \chi) = (2000, 500)$ as the reference solution, let $K_{\zeta, \chi}$ denote the kinetic energy obtained with stabilization parameters (ζ, χ) . We then define

$$\delta_K(\zeta, \chi) = \frac{\int_0^T |K_{\zeta, \chi}(t) - K_{2000, 500}(t)| dt}{\int_0^T |K_{2000, 500}(t)| dt}$$

and similarly for δ_M , δ_Z , and δ_J .

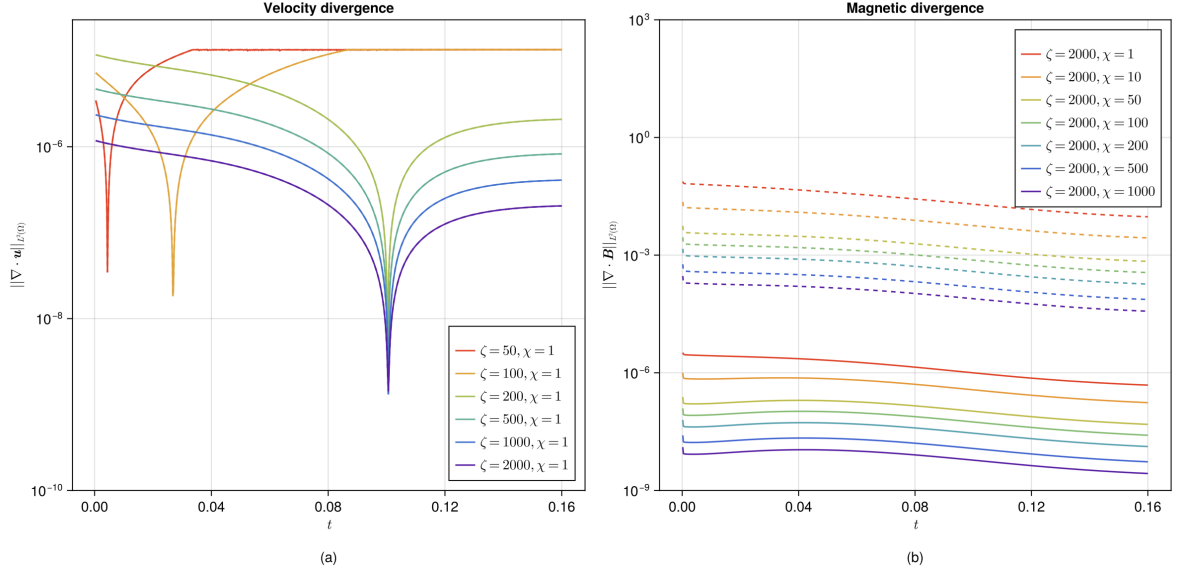


Figure 4: Time evolution of the divergence norms in the linear ramp case (Case 2) used for selecting the stabilization parameters. **(a)** $\|\nabla \cdot \mathbf{u}_h\|$ for several values of ζ with $\chi = 1$; **(b)** $\|\nabla \cdot \mathbf{B}_h\|$ for several values of χ with $\zeta = 2000$. Dashed lines correspond to the values before cleaning and solid lines correspond to the values after cleaning.

The corresponding results are collected in Table 4. Increasing ζ from 50 to 2000 with $\chi = 1$ reduces $\max_n \|\nabla \cdot \mathbf{u}_h^n\|$ from 1.35×10^{-5} to 1.18×10^{-6} , while $\max_n \|\nabla \cdot \mathbf{B}_h^n\|$ remains unchanged. After fixing $\zeta = 2000$, increasing χ from 1 to 500 reduces $\max_n \|\nabla \cdot \mathbf{B}_h^n\|$ from 3.27×10^{-6} to 2.53×10^{-8} , whereas $\max_n \|\nabla \cdot \mathbf{u}_h^n\|$ stays nearly the same. At the same time, the relative differences δ_K , δ_M , δ_Z , and δ_J remain very small for all tested parameters. In particular, all of them are below 10^{-3} , and for the larger values of χ they are much smaller. This shows that the stabilization parameters have a strong effect on the divergence norms, while their influence on the kinetic energy, magnetic energy, enstrophy, and current enstrophy is negligible on the scale of the present simulations.

Table 4: Maximum divergence norms and relative differences in the kinetic energy, magnetic energy, enstrophy, and current enstrophy corresponding to different stabilization parameters. The quantities δ_K , δ_M , δ_Z , and δ_J are defined with respect to the reference run with $(\zeta, \chi) = (2000, 500)$.

(ζ, χ)	$\max_n \ \nabla \cdot \mathbf{u}_h^n\ $	$\max_n \ \nabla \cdot \mathbf{B}_h^n\ $	δ_K	δ_M	δ_Z	δ_J
(50, 1)	1.3499×10^{-5}	3.2658×10^{-6}	3.9153×10^{-4}	7.7490×10^{-4}	1.5204×10^{-4}	8.7946×10^{-4}
(100, 1)	1.3499×10^{-5}	3.2658×10^{-6}	3.9153×10^{-4}	7.7490×10^{-4}	1.5204×10^{-4}	8.7946×10^{-4}
(200, 1)	1.1755×10^{-5}	3.2658×10^{-6}	3.9152×10^{-4}	7.7490×10^{-4}	1.5204×10^{-4}	8.7945×10^{-4}
(500, 1)	4.7040×10^{-6}	3.2658×10^{-6}	3.9152×10^{-4}	7.7490×10^{-4}	1.5204×10^{-4}	8.7946×10^{-4}
(1000, 1)	2.3524×10^{-6}	3.2658×10^{-6}	3.9152×10^{-4}	7.7490×10^{-4}	1.5204×10^{-4}	8.7946×10^{-4}
(2000, 1)	1.1763×10^{-6}	3.2658×10^{-6}	3.9152×10^{-4}	7.7490×10^{-4}	1.5204×10^{-4}	8.7946×10^{-4}
(2000, 10)	1.1792×10^{-6}	9.8632×10^{-7}	1.0414×10^{-4}	2.0551×10^{-4}	6.0049×10^{-5}	2.3292×10^{-4}
(2000, 50)	1.1800×10^{-6}	2.4044×10^{-7}	2.3135×10^{-5}	4.5478×10^{-5}	1.4729×10^{-5}	5.1350×10^{-5}
(2000, 100)	1.1801×10^{-6}	1.2360×10^{-7}	1.0572×10^{-5}	2.0777×10^{-5}	6.8492×10^{-6}	2.3434×10^{-5}
(2000, 200)	1.1802×10^{-6}	6.2682×10^{-8}	4.0218×10^{-6}	7.9036×10^{-6}	2.6305×10^{-6}	8.9081×10^{-6}
(2000, 500)	1.1802×10^{-6}	2.5289×10^{-8}	—	—	—	—
(2000, 1000)	1.1802×10^{-6}	1.2681×10^{-8}	1.3563×10^{-6}	2.6655×10^{-6}	8.9438×10^{-7}	3.0025×10^{-6}

3.3.2 Impact of Constant-order Fractional Derivatives on Energy-Enstrophy Measures

We begin by analyzing Case 1. Figure 5 shows the effect of the constant fractional order α on the kinetic energy $K(t)$, magnetic energy $M(t)$, enstrophy $Z(t)$, and current enstrophy $J(t)$. The dependence on α is clearest in the magnetic quantities $M(t)$ and $J(t)$. In both plots, the classical case stays above all fractional cases, and smaller values of α lead to faster decay over the whole interval.

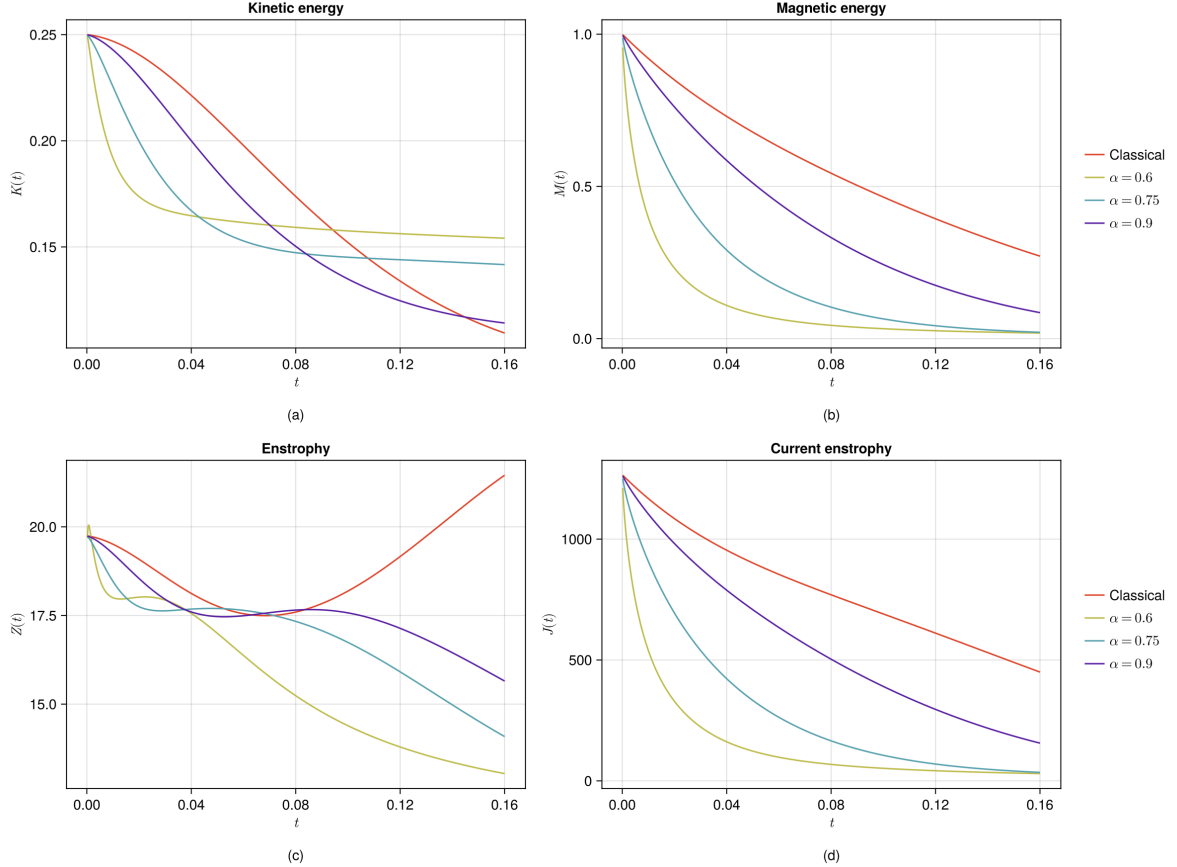


Figure 5: Comparison of the diagnostics for the classical model ($\alpha(t) = \beta(t) \equiv 1$) and the constant-order fractional cases, showing the effect of α on the evolution of the main energy and enstrophy measures: (a) Kinetic energy $K(t)$; (b) Magnetic energy $M(t)$; (c) Enstrophy $Z(t)$; (d) Current enstrophy $J(t)$.

The kinetic energy $K(t)$ behaves differently. The cases $\alpha = 0.6$ and $\alpha = 0.75$ decrease faster at early times, but later their curves become flatter and stay above the classical one. The case $\alpha = 0.9$ remains closer to the classical curve, although it also ends above it near the final time. Thus, the influence of α on $K(t)$ is not the same over the whole interval.

The enstrophy $Z(t)$ shows a clear difference between the classical and fractional cases. In the classical case, $Z(t)$ first decreases, reaches a minimum near the middle of the interval, and then increases strongly toward the final time. In all fractional cases, this final increase is absent, and the curves remain below the classical one in the second half of the interval.

There are also visible differences among the fractional cases themselves. For $\alpha = 0.6$, the enstrophy drops most rapidly at early times and then continues to decrease after a short intermediate flattening. For $\alpha = 0.75$, the behavior is similar, but the decrease is less steep and the flatter part is more pronounced. The case $\alpha = 0.9$ stays closest to the classical curve for the longest time: after the initial decrease, it shows a mild increase around the middle of the

interval, and only later turns downward. Thus, smaller values of α lead to an earlier and stronger reduction of enstrophy, while values closer to 1 retain a profile more similar to the classical one.

3.3.3 Impact of Variable-order Fractional Derivatives on Energy-Enstrophy Measures

Figure 6 compares the variable-order profiles (Cases 2–5) with the classical model using the same diagnostics. In all four cases, the magnetic energy $M(t)$ and the current enstrophy $J(t)$ decay much faster than in the classical solution. At the same time, the variable-order curves are not identical, which shows that the results depend not only on the values of $\alpha(t)$, but also on how $\alpha(t)$ changes in time.

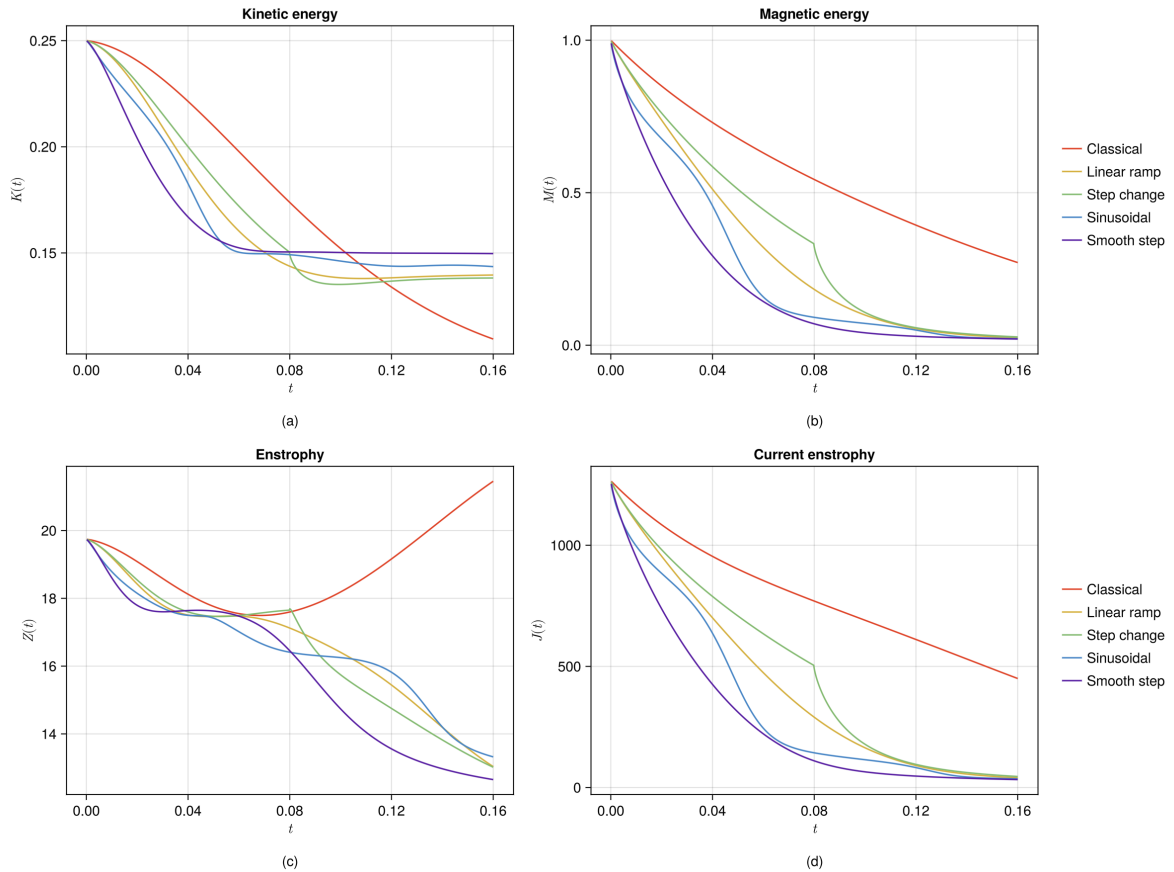


Figure 6: Comparison of the diagnostics across classical model ($\alpha \equiv 1$) and variable-order fractional cases, showing the effect of $\alpha(t)$ on energy levels and small-scale activity: **(a)** Kinetic energy $K(t)$; **(b)** Magnetic energy $M(t)$; **(c)** Enstrophy $Z(t)$; **(d)** Current enstrophy $J(t)$.

These differences are most visible in $M(t)$ and $J(t)$. In the linear-ramp case, both quantities decrease smoothly. In the step-change case, the decay becomes steeper after the switching time. The smooth-step case behaves similarly, but the change is more gradual. The sinusoidal case is different from the others: both $M(t)$ and $J(t)$ show a flatter middle part before continuing to decrease.

The kinetic energy $K(t)$ behaves differently. All variable-order cases decrease faster than the classical one at early times, but later they flatten and remain above the classical curve. The smooth-step case stays highest at later times, while the linear-ramp, step-change, and sinusoidal cases remain closer to each other.

The enstrophy $Z(t)$ also differs clearly from the classical case. In the classical solution, it

first decreases and then grows strongly near the final time. This final growth is absent in all variable-order cases. The linear-ramp case decreases rather regularly after the initial stage. The step-change case stays close to it at first and then drops faster after the change in order. The sinusoidal case remains higher for longer in the middle of the interval, while the smooth-step case decreases more steadily and reaches the smallest values near the end.

3.3.4 The Case of Asynchronous (Unsymmetrical) Variable Orders

In this experiment, we consider six configurations in which $\alpha(t)$ and $\beta(t)$ vary independently. Each configuration is denoted AR-XY, where $X \in \{U, D, C\}$ describes the trend of $\alpha(t)$, $Y \in \{U, D, C\}$ describes the trend of $\beta(t)$, and U, D, and C denote increasing, decreasing, and constant profiles, respectively:

$$\text{Case AR-UD: } \alpha(t) = 0.6 + \frac{0.3t}{T}, \beta(t) = 0.9 - \frac{0.3t}{T}.$$

$$\text{Case AR-DU: } \alpha(t) = 0.9 - \frac{0.3t}{T}, \beta(t) = 0.6 + \frac{0.3t}{T}.$$

$$\text{Case AR-UC: } \alpha(t) = 0.6 + \frac{0.3t}{T}, \beta(t) = 0.75.$$

$$\text{Case AR-DC: } \alpha(t) = 0.9 - \frac{0.3t}{T}, \beta(t) = 0.75.$$

$$\text{Case AR-CU: } \alpha(t) = 0.75, \beta(t) = 0.6 + \frac{0.3t}{T}.$$

$$\text{Case AR-CD: } \alpha(t) = 0.75, \beta(t) = 0.9 - \frac{0.3t}{T}.$$

Figure 7 compares the classical model with six cases in which $\alpha(t)$ and $\beta(t)$ evolve differently. In all six cases, the fractional curves separate from the classical one soon after $t = 0$, so varying $\alpha(t)$ and $\beta(t)$ independently affects all four diagnostics.

The kinetic energy $K(t)$ shows a clear spread among the fractional cases. At later times, the largest values are attained by AR-DU and AR-CU, while the smallest values are given by AR-UD. The cases AR-UC and AR-DC lie between these two groups, and AR-CD ends close to AR-UC. Thus, the late-time values of $K(t)$ differ noticeably from one profile to another.

The magnetic energy $M(t)$ and the current enstrophy $J(t)$ show a clearer pattern. In all six fractional cases, both quantities decay much faster than in the classical solution. The slowest decay among the fractional runs is observed for AR-UD and AR-CD, which remain closest to the classical curve. The fastest decay is seen for AR-DU and AR-CU. The remaining two cases, AR-UC and AR-DC, stay between these groups. The same grouping is visible in both $M(t)$ and $J(t)$.

The enstrophy $Z(t)$ also differs clearly from the classical case. In the classical solution, it decreases at first and then grows strongly near the final time. This final growth is absent in all six fractional cases. Among them, AR-DU reaches the highest values in the middle part of the interval, followed by AR-CU and AR-DC. The cases AR-UC and AR-CD remain lower, while AR-UD stays lowest for most of the interval and decreases most strongly toward the end.

Overall, the plots show that allowing $\alpha(t)$ and $\beta(t)$ to evolve differently changes not only the size of the magnetic quantities, but also the relative behavior of the velocity-related diagnostics. The clearest separation appears again in $M(t)$ and $J(t)$, while $K(t)$ and $Z(t)$ show a wider spread between the different profiles.

3.3.5 Analysis of Relative Changes in Integral and Peak Quantities

To summarize the influence of the fractional orders on the global diagnostics, we introduce the relative $L^1(0, T)$ deviation

$$\Delta K = \frac{\int_0^T |K_\alpha(t) - K_1(t)| dt}{\int_0^T |K_1(t)| dt},$$

where $K_\alpha(t)$ and $K_1(t)$ denote the kinetic energy in the fractional and classical cases, respectively. The quantities ΔM , ΔZ , and ΔJ are defined in the same way for the magnetic energy, enstrophy, and current enstrophy. The values are listed in Table 5.

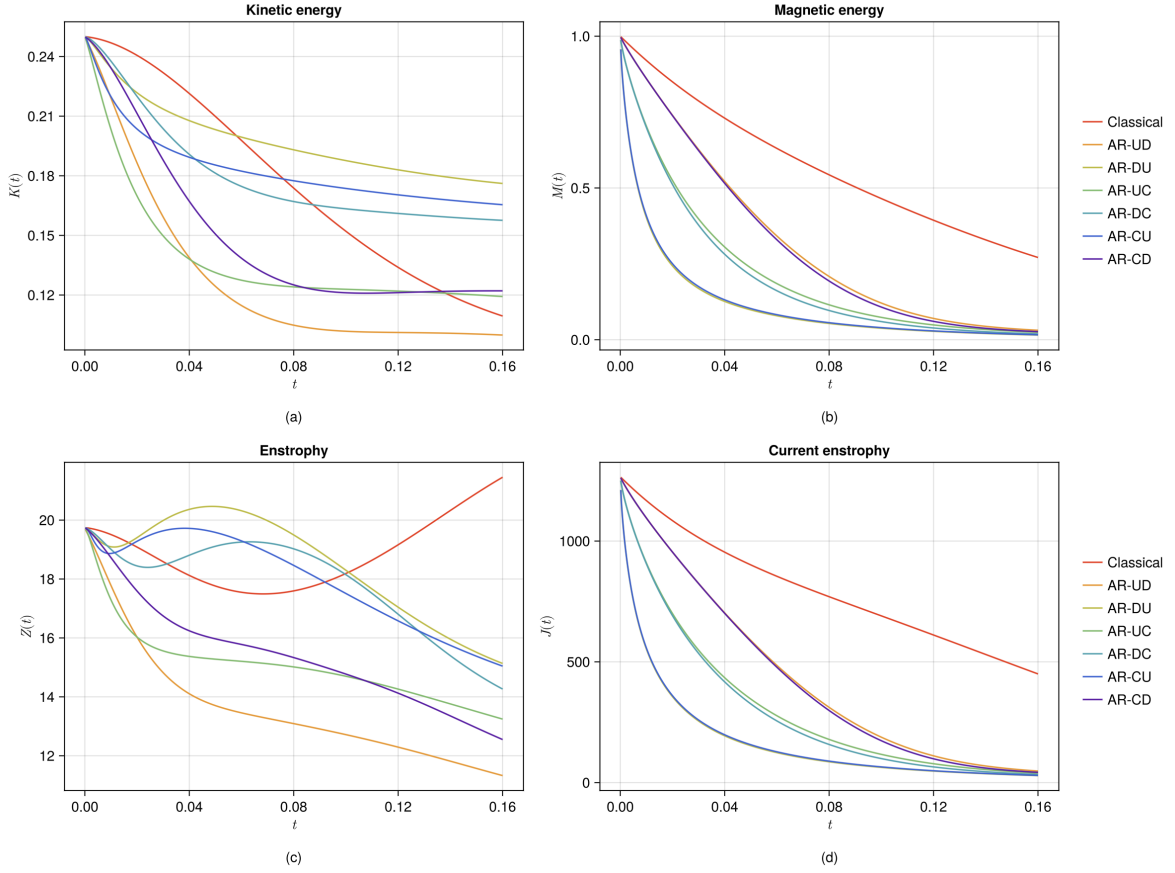


Figure 7: Comparison of the diagnostics across classical model ($\alpha(t) = \beta(t) \equiv 1$) and unsymmetric variable-order fractional cases, showing the effect of $\alpha(t) = \beta(t)$ on energy levels and small-scale activity: (a) Kinetic energy $K(t)$; (b) Magnetic energy $M(t)$; (c) Enstrophy $Z(t)$; (d) Current enstrophy $J(t)$.

For the constant-order cases, all four deviations decrease as α increases from 0.6 to 0.9. Thus, in the constant-order case, the cumulative difference from the classical case decreases as the order approaches 1.

Among the symmetric variable-order cases (Cases 2–5), the step-change profile gives the smallest values of ΔK , ΔM , and ΔJ , while the smooth-step profile gives the largest values of these quantities. The linear-ramp and sinusoidal cases lie between these two. In all four cases, ΔM and ΔJ are clearly larger than ΔK and ΔZ , which confirms that the magnetic diagnostics are more sensitive than the kinetic ones.

The asynchronous cases (Case 6) show a different pattern. The largest kinetic deviation is obtained for AR-UD, followed by AR-UC, whereas the largest magnetic deviations are obtained for AR-DU and AR-CU. The cases AR-UC and AR-DC lie between these extremes, while AR-CD remains closer to AR-UD in the magnetic diagnostics. The enstrophy deviations also vary noticeably, with the largest value attained by AR-UD. It follows from the table that once $\alpha(t)$ and $\beta(t)$ vary independently, the cumulative deviation from the classical solution is no longer described by a single common trend. Some profiles produce the largest changes in the kinetic energy and enstrophy, whereas others produce the largest changes in the magnetic energy and current enstrophy.

Table 5: Relative differences in the integral diagnostics with respect to the classical model ($\alpha(t) \equiv 1$, $\beta(t) \equiv 1$).

Case	ΔK	ΔM	ΔZ	ΔJ
Constant-order (Case 1), $\alpha(t) \equiv 0.6$	0.1923	0.8121	0.1721	0.8080
Constant-order (Case 1), $\alpha(t) \equiv 0.75$	0.1577	0.6363	0.1053	0.6314
Constant-order (Case 1), $\alpha(t) \equiv 0.9$	0.0783	0.3028	0.0697	0.2912
Linear ramp (Case 2)	0.1150	0.4689	0.1165	0.4717
Step change (Case 3)	0.0961	0.3924	0.1254	0.3983
Sinusoidal (Case 4)	0.1341	0.5664	0.1246	0.5701
Smooth step (Case 5)	0.1624	0.6481	0.1584	0.6490
Asynchronous ramp (Case 6), AR-UD	0.2821	0.4447	0.2774	0.4564
Asynchronous ramp (Case 6), AR-DU	0.1647	0.7990	0.1153	0.7884
Asynchronous ramp (Case 6), AR-UC	0.2321	0.6208	0.2001	0.6199
Asynchronous ramp (Case 6), AR-DC	0.1282	0.6455	0.1026	0.6374
Asynchronous ramp (Case 6), AR-CU	0.1605	0.7937	0.1039	0.7852
Asynchronous ramp (Case 6), AR-CD	0.1723	0.4592	0.1810	0.4660

3.3.6 Influence of the Reynolds Numbers on Energy-Enstrophy Measures

Figure 8 shows the influence of the Reynolds numbers $\text{Re} = \text{Rm}$ on the diagnostics for the linear-ramp case (Case 2). The clearest effect is seen in the magnetic energy $M(t)$ and the current enstrophy $J(t)$. As $\text{Re} = \text{Rm}$ increases from 100 to 700, both quantities decay more slowly, and their curves remain successively higher over the whole time interval.

The kinetic energy $K(t)$ behaves differently. After a short initial stage, the case $\text{Re} = \text{Rm} = 100$ stays above the others over most of the interval. Among the cases $\text{Re} = \text{Rm} = 300, 500, 700$, the larger Reynolds numbers generally give smaller values of $K(t)$ over most of the time interval.

The enstrophy $Z(t)$ shows a different pattern. For $\text{Re} = \text{Rm} = 100$, it decreases over the whole interval. For $\text{Re} = \text{Rm} = 300$, the curve first decreases, then shows a mild rise, and finally decreases again. For $\text{Re} = \text{Rm} = 500$ and 700, this rise becomes much more pronounced, and the largest peak is reached for $\text{Re} = \text{Rm} = 700$.

Thus, increasing Re and Rm slows down the decay of $M(t)$ and $J(t)$. The effect on $K(t)$ is different and is not ordered in the same way. For $Z(t)$, larger Reynolds numbers lead to a stronger rise at intermediate times and to a higher peak before the final decay.

3.3.7 Analysis of the Divergence Constraints

Figure 9 shows the time evolution of the divergence norms for the variable-order profiles considered in the tests above. In all cases, the velocity divergence $\|\nabla \cdot \mathbf{u}_h\|$ remains small over the whole interval. Its values are of order 10^{-6} at early times, decrease further around the middle of the simulation, and then remain at the level of 10^{-7} . Although the detailed shape depends on the chosen order profile, no growth to large values is observed.

For the magnetic field, both the values before cleaning and the values after cleaning are shown. Before cleaning, $\|\nabla \cdot \mathbf{B}_h\|$ stays at the level of 10^{-4} throughout the interval. After cleaning, it is reduced to the level of 10^{-8} for all considered profiles. In both cases, the curves remain bounded and show only moderate variation in time. Thus, for all variable-order functions used in the computations below, the divergence errors remain under control during the whole simulation interval.

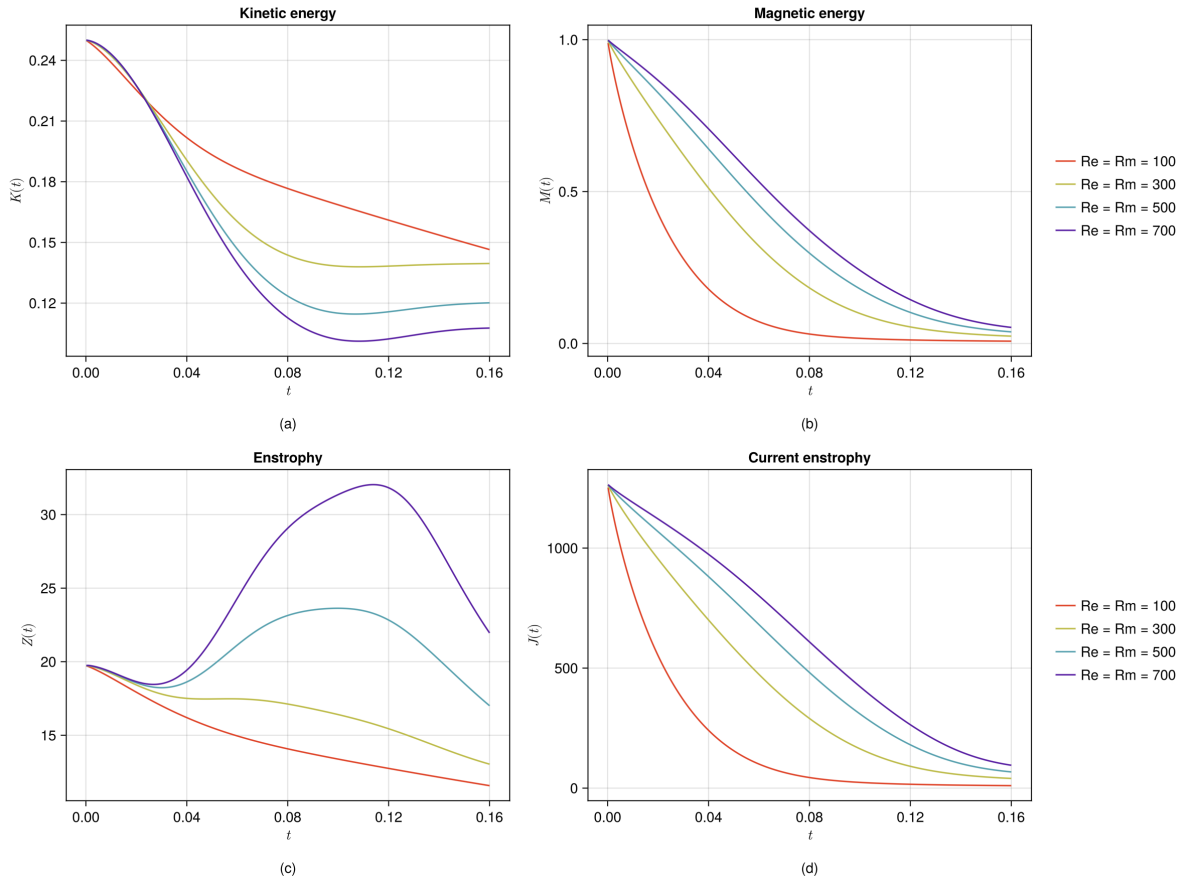


Figure 8: Comparison of the diagnostics across different values of the Reynolds numbers $\text{Re} = \text{Rm}$: **(a)** Kinetic energy $K(t)$; **(b)** Magnetic energy $M(t)$; **(c)** Enstrophy $Z(t)$; **(d)** Current enstrophy $J(t)$.

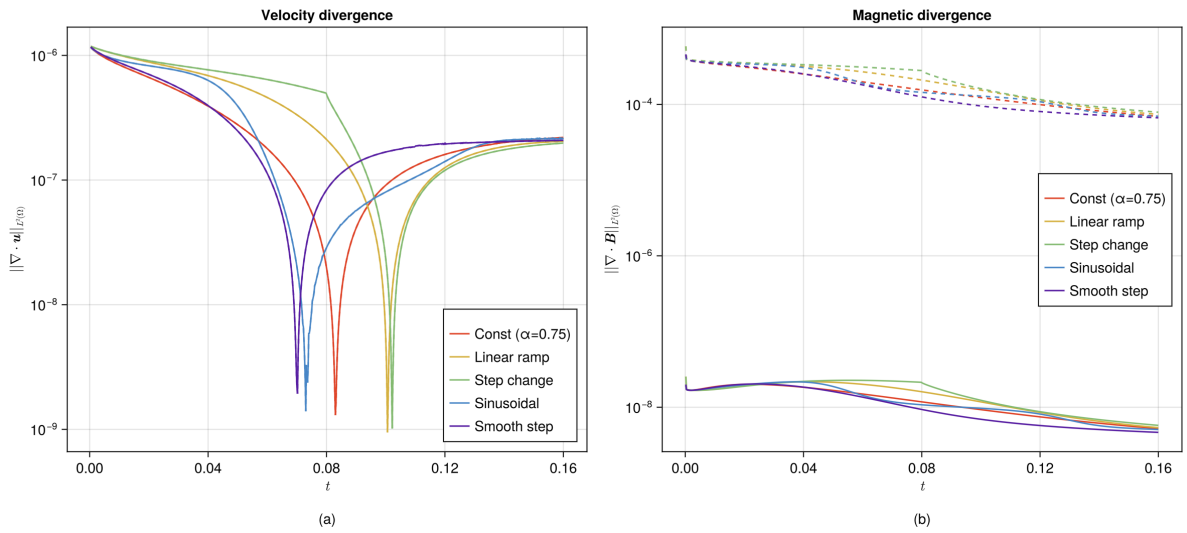


Figure 9: Time evolution of the divergence norms for several representative variable-order profiles. **(a)** Velocity divergence $\|\nabla \cdot \mathbf{u}_h\|$. **(b)** Magnetic divergence $\|\nabla \cdot \mathbf{B}_h\|$, with dashed lines corresponding to the values before cleaning and solid lines to the values after cleaning.

3.4 Phase Diagrams in the Order-Range Plane

We next investigate how the initial and final values of the variable-order temporal fractional derivative, denoted by (α_0, α_T) , influence diagnostics of the MHD flow. In this experiment, (α_0, α_T) are the endpoints of the linear-ramp profile

$$\alpha(t) = \beta(t) = \alpha_0 + (\alpha_T - \alpha_0) \frac{t}{T}, \quad t \in [0, T], \quad (50)$$

with $T = 0.16$, so that $\alpha(0) = \alpha_0$ and $\alpha(T) = \alpha_T$. The initial and boundary data, as well as all remaining parameters, are the same as in Section 3.3.

For each pair (α_0, α_T) on the grid $0.5 \leq \alpha_0 \leq 0.9$, $0.5 \leq \alpha_T \leq 0.9$ we compute the time histories of the diagnostic quantities $K(t)$, $M(t)$, $Z(t)$, and $J(t)$, and then evaluate their time integrals

$$I_K = \int_0^T K(t) dt, \quad I_M = \int_0^T M(t) dt, \quad I_Z = \int_0^T Z(t) dt, \quad I_J = \int_0^T J(t) dt.$$

To measure the effect of (α_0, α_T) , we compare these quantities with the classical reference solution and define

$$\delta I_K = \frac{I_K - I_K^{\text{ref}}}{I_K^{\text{ref}}}, \quad \delta I_M = \frac{I_M - I_M^{\text{ref}}}{I_M^{\text{ref}}}, \quad \delta I_Z = \frac{I_Z - I_Z^{\text{ref}}}{I_Z^{\text{ref}}}, \quad \delta I_J = \frac{I_J - I_J^{\text{ref}}}{I_J^{\text{ref}}}.$$

The heatmaps in Figure 10 summarize how these relative deviations vary over the (α_0, α_T) -plane.

The heatmaps show that all four quantities satisfy $\delta I_K < 0$, $\delta I_M < 0$, $\delta I_Z < 0$, and $\delta I_J < 0$ throughout the tested range. Therefore, for all considered ramp profiles, the time-integrated kinetic energy, magnetic energy, enstrophy, and current enstrophy are smaller than in the classical case. The largest changes appear in I_J and I_Z . The changes in I_M are also visible but smaller, whereas the changes in I_K are much weaker.

The dependence on (α_0, α_T) is clearest in δI_M , δI_Z , and δI_J . In these three maps, the deviations become more negative when the order range moves toward smaller values, and less negative as (α_0, α_T) approaches $(0.9, 0.9)$. For δI_K , the same pattern is only weakly visible and is less regular.

Taken together, these maps show that the order range (α_0, α_T) affects all four integrated diagnostics. The values of I_M , I_Z , and I_J are the most sensitive among those considered, while I_K is the least sensitive.

4 Discussion

The results obtained in this work show that replacing the integer-order time derivatives in the incompressible MHD system with variable-order Caputo derivatives allows a wider range of transient behaviors to be described within the same governing equations. From a physical point of view, the variable-order fractional terms introduce a memory effect whose strength changes in time. In qualitative terms, smaller fractional orders correspond to stronger temporal memory, whereas values closer to unity lead to behavior that is closer to the classical incompressible MHD model. In this way, the order functions $\alpha(t)$ and $\beta(t)$ can be used to describe time-dependent changes in memory strength.

Although the variable-order fractional MHD tests considered here do not use exactly the same initial data as many standard benchmark studies [13, 22, 25], two qualitative checks are still useful. First, in the classical case $\alpha(t), \beta(t) \equiv 1$, the computed solution shows the expected dissipative behavior of a periodic divergence-free MHD vortex: the kinetic and magnetic energies decay in time, while the enstrophy and current-enstrophy curves provide additional information on the evolution of velocity and magnetic gradients. Such qualitative diagnostics are often used

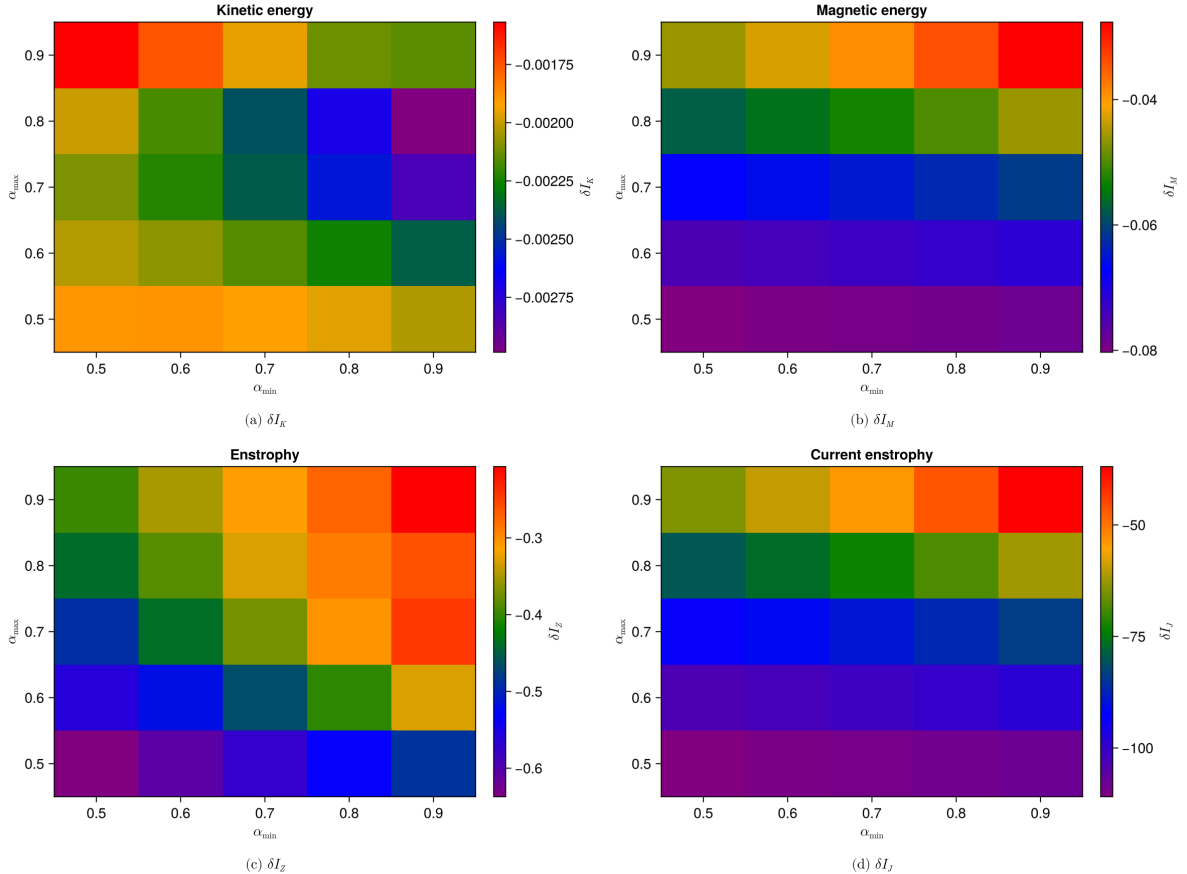


Figure 10: Heatmaps of the relative deviations of the time-integrated diagnostics for the linear-ramp profile (50). The horizontal and vertical axes correspond to the values of α_0 and α_T , respectively. **(a)** δI_K , relative deviation of the time-integrated kinetic energy; **(b)** δI_M , relative deviation of the time-integrated magnetic energy; **(c)** δI_Z , relative deviation of the time-integrated enstrophy; **(d)** δI_J , relative deviation of the time-integrated current enstrophy. All quantities are computed relative to the classical reference solution.

in the MHD literature when assessing numerical solvers on periodic vortex-type problems [20, 23, 40]. Therefore, the run with $\alpha(t), \beta(t) \equiv 1$ provides a consistent reference for interpreting the fractional-order cases computed with the same discretization, parameters, and diagnostics.

Second, varying the fractional order produces visible changes in all diagnostics over the whole time interval. These changes are seen in the levels of the curves and, in particular for Z and J , in the timing of the transient extrema. When $\alpha(t)$ and $\beta(t)$ remain close to 1, the diagnostics stay closer to the classical solution. Lower orders, or stronger variation in time, lead to larger deviations and more noticeable shifts in the extrema. This suggests that variable-order memory affects both the overall level of the diagnostics and the transient development of the flow.

Similar sensitivity to the order profile has also been reported in other variable-order fractional flow models. For example, porous-media studies [6] comparing constant, increasing, and decreasing orders show that different choices of the order function can lead to visibly different flow responses. Although the governing equations in those models differ from the present incompressible MHD system, the qualitative point is similar: changing the order profile modifies the strength of the memory effect and thereby changes the transient evolution.

Finally, we recall that the present H^1 -conforming discretization does not enforce the divergence constraints exactly at the discrete level. Therefore, the divergence norms reported in this work are expected to be small but not identically zero. In the convergence tests, moder-

ate stabilization parameters were sufficient to keep these quantities small, while in the periodic divergence-free vortex test larger stabilization parameters were used to obtain smaller divergence errors in the nonlinear case.

The main limitation of the present study is that the numerical investigation has been carried out for a finite set of order functions. A natural extension is to consider a broader class of variable-order profiles $\alpha(t)$ and $\beta(t)$, including dependencies on spatial variables. Another important direction is comparison with experimental data or with high-accuracy numerical simulations for classical MHD.

5 Conclusions

This work studied a variable-order time-fractional incompressible MHD model in which the classical first-order time derivatives in the momentum and induction equations are replaced by Caputo derivatives with time-dependent order. For the resulting problem, a fully discrete finite element–L1 scheme was proposed and analyzed through stability and convergence results. The scheme was then examined numerically by means of convergence tests, a classical-limit study as the orders approach unity, computations for the periodic divergence-free vortex, and order-range sensitivity maps for selected diagnostics.

The numerical results lead to several main observations. First, the finite element–L1 discretization shows the expected temporal behavior for the representative variable-order profiles considered in this work. Second, the classical-limit test confirms consistency with the standard incompressible MHD model: as the fractional orders approach one, the differences between the fractional and classical solutions decrease, and the corresponding diagnostic curves become closer. Third, in the periodic divergence-free vortex test, changing the order functions produces clear changes in the kinetic and magnetic energies, enstrophy, and current-related diagnostics. Finally, the order-range maps show how these diagnostics vary over the (α_0, α_T) -plane and indicate regions where the influence of variable order is stronger or weaker.

Taken together, these results show that variable-order Caputo time derivatives provide a useful way to describe time-dependent memory effects in incompressible MHD while remaining consistent with the classical limit. Future work will include the study of broader classes of order functions in the momentum and induction equations, additional benchmark problems and boundary conditions, extension of the analysis to more general variable-order cases, and acceleration techniques for long-time simulations.

Acknowledgements

This research was funded by the Science Committee of the Ministry of Science and Higher Education of the Republic of Kazakhstan (Grant No. AP26101983).

Appendix A. Discrete fractional Grönwall inequality

For the reader’s convenience, we restate the kernel assumptions and the discrete fractional Grönwall theorem of [28] below in notation adapted to the present paper.

Let $0 = t_0 < t_1 < \dots < t_N = T$, $\tau_n = t_n - t_{n-1}$, let $0 \leq \theta < 1$, and let $\gamma \in (0, 1)$. For any sequence $\{v^n\}_{n=0}^N$, define

$$t_{n-\theta} = \theta t_{n-1} + (1 - \theta) t_n, \quad v^{n-\theta} = \theta v^{n-1} + (1 - \theta) v^n, \quad \nabla_\tau v^n = v^n - v^{n-1}.$$

Consider a discrete fractional derivative of convolution type,

$$(\mathcal{D}_\tau^\gamma v)^{n-\theta} = \sum_{k=1}^n A_{n-k}^{(n)} \nabla_\tau v^k, \quad 1 \leq n \leq N,$$

where the coefficients $A_{n-k}^{(n)}$ are referred to as discrete convolution kernels. The abstract theory of [28] is formulated for kernels of this form under the following structural assumptions.

Assumption A1. For each fixed n , the kernel sequence is positive and nonincreasing:

$$A_0^{(n)} \geq A_1^{(n)} \geq A_2^{(n)} \geq \dots \geq A_{n-1}^{(n)} > 0.$$

Assumption A2. There exists a constant $\pi_A > 0$, independent of the time steps, such that

$$A_{n-k}^{(n)} \geq \frac{1}{\pi_A \tau_k} \int_{t_{k-1}}^{t_k} \omega_{1-\gamma}(t_n - s) ds, \quad 1 \leq k \leq n \leq N,$$

where $\omega_{1-\gamma}(t) = \frac{t^{-\gamma}}{\Gamma(1-\gamma)}$.

Assumption A3. There exists a constant $\rho > 0$ such that the local step ratios satisfy

$$\rho_k = \frac{\tau_k}{\tau_{k+1}} \leq \rho, \quad 1 \leq k \leq N-1.$$

When A1–A2 hold, one defines the associated complementary kernels $\{\mathcal{P}_{n-j}^{(n)}\}$ recursively by the identity

$$\sum_{j=m}^n \mathcal{P}_{n-j}^{(n)} A_{j-m}^{(j)} = 1, \quad 1 \leq m \leq n \leq N.$$

Theorem (Discrete fractional Grönwall inequality). Assume that A1–A3 hold. Let $\{g^n\}_{n=1}^N$ and $\{\lambda_\ell\}_{\ell=0}^{N-1}$ be nonnegative sequences, and suppose that there exists a constant Λ , independent of the time steps, such that $\Lambda \geq \sum_{\ell=0}^{N-1} \lambda_\ell$. Assume further that the maximum time step satisfies

$$\max_{1 \leq n \leq N} \tau_n \leq (2\pi_A \Gamma(2-\gamma) \Lambda)^{-1/\gamma}.$$

If a nonnegative sequence $\{v^n\}_{n=0}^N$ satisfies

$$\sum_{k=1}^n A_{n-k}^{(n)} \nabla_\tau v^k \leq \sum_{k=1}^n \lambda_{n-k} v^{k-\theta} + g^n, \quad 1 \leq n \leq N,$$

then, for every $1 \leq n \leq N$,

$$v^n \leq 2\mathbb{E}_\gamma(2 \max(1, \rho) \pi_A \Lambda t_n^\gamma) \left(v^0 + \max_{1 \leq k \leq n} \sum_{j=1}^k \mathcal{P}_{k-j}^{(k)} g^j \right),$$

where \mathbb{E}_γ denotes the Mittag–Leffler function.

Remark. By Remark 1 of [28], under Assumptions A1–A2 the complementary kernels satisfy

$$\sum_{j=1}^k \mathcal{P}_{k-j}^{(k)} \omega_{1-\gamma}(t_j) \leq \pi_A, \quad 1 \leq k \leq N.$$

Hence

$$\sum_{j=1}^k \mathcal{P}_{k-j}^{(k)} g^j \leq \pi_A \max_{1 \leq j \leq k} \frac{g^j}{\omega_{1-\gamma}(t_j)} = \pi_A \Gamma(1-\gamma) \max_{1 \leq j \leq k} (t_j^\gamma g^j), \quad 1 \leq k \leq N.$$

In particular, if $g^j \equiv g$ is independent of j , then

$$\sum_{j=1}^k \mathcal{P}_{k-j}^{(k)} g \leq \pi_A \Gamma(1-\gamma) t_k^\gamma g \leq \pi_A \Gamma(1-\gamma) T^\gamma g.$$

References

- [1] Abbas, S., Nisa, Z.U., Gilani, S.F.F., Nazar, M., Metwally, A.S.M., Jan, A.Z., 2024. Fractional analysis of magnetohydrodynamics Maxwell flow over an inclined plate with the effect of thermal radiation. *International Journal of Theoretical Physics* 63. doi:[10.1007/s10773-024-05654-3](https://doi.org/10.1007/s10773-024-05654-3).
- [2] Abdiramanov, Z.A., Baishemirov, Z.D., Berdyshev, A.S., Shiyapov, K.M., 2024. An implicit difference scheme for a mixed problem of hyperbolic type with memory. *Lobachevskii Journal of Mathematics* 45, 569–577. doi:[10.1134/s1995080224600249](https://doi.org/10.1134/s1995080224600249).
- [3] Abylkairov, U.U., Aitzhanov, S.E., 2015. Inverse problem for non-stationary system of magnetohydrodynamics. *Boundary Value Problems* 2015. doi:[10.1186/s13661-015-0438-x](https://doi.org/10.1186/s13661-015-0438-x).
- [4] Agilan, K., Naveen, S., Suganya, S., Parthiban, V., 2025. Analysis of variable-order fractional enzyme kinetics model with time delay. *Scientific Reports* 15. doi:[10.1038/s41598-025-16382-x](https://doi.org/10.1038/s41598-025-16382-x).
- [5] Ali, Q., Amir, M., Metwally, A.S.M., Younas, U., Jan, A.Z., Amjad, A., 2024. Investigation of MHD fractionalized viscous fluid and thermal memory with slip and Newtonian heating effect: a fractional model based on Mittag-Leffler kernel. *Journal of Thermal Analysis and Calorimetry* 149, 8257–8270. doi:[10.1007/s10973-024-13205-5](https://doi.org/10.1007/s10973-024-13205-5).
- [6] Alimbekova, N., Bakishev, A., Berdyshev, A., 2024. Numerical method for the variable-order fractional filtration equation in heterogeneous media. *Fractal and Fractional* 8, 640. doi:[10.3390/fractalfract8110640](https://doi.org/10.3390/fractalfract8110640).
- [7] Altybay, A., 2026. Numerical identification of a time-dependent coefficient in a time-fractional diffusion equation with integral constraints. *Zeitschrift für angewandte Mathematik und Physik* 77. doi:[10.1007/s00033-025-02653-0](https://doi.org/10.1007/s00033-025-02653-0).
- [8] Arif, M., Kumam, P., Seangwattana, T., Suttiarporn, P., 2023. A fractional model of magnetohydrodynamics Oldroyd-B fluid with couple stresses, heat and mass transfer: A comparison among non-Newtonian fluid models. *Heliyon* 9, e17642. doi:[10.1016/j.heliyon.2023.e17642](https://doi.org/10.1016/j.heliyon.2023.e17642).
- [9] Asai, S., 2011. *Magnetohydrodynamics in Materials Processing*. Springer Netherlands. pp. 49–86. doi:[10.1007/978-94-007-2645-1_3](https://doi.org/10.1007/978-94-007-2645-1_3).
- [10] Asjad, M.I., Usman, M., Assiri, T.A., Ali, A., Tag-ElDin, E.M., 2023. Numerical investigation of fractional Maxwell nano-fluids between two coaxial cylinders via the finite difference approach. *Frontiers in Materials* 9. doi:[10.3389/fmats.2022.1050767](https://doi.org/10.3389/fmats.2022.1050767).
- [11] Bader, S.H., Zhu, X., 2025. AFiD-MHD: A finite difference method for magnetohydrodynamic flows. *Journal of Computational Physics* 523, 113658. doi:[10.1016/j.jcp.2024.113658](https://doi.org/10.1016/j.jcp.2024.113658).
- [12] Baishemirov, Z., Berdyshev, A., Baigereyev, D., Boranbek, K., 2024. Efficient numerical implementation of the time-fractional stochastic Stokes–Darcy model. *Fractal and Fractional* 8, 476. doi:[10.3390/fractalfract8080476](https://doi.org/10.3390/fractalfract8080476).
- [13] Borge, S., Omang, M., Trulsen, J., 2006. Multidimensional MHD shock tests of regularized smoothed particle hydrodynamics. *The Astrophysical Journal* 652, 1306–1317. doi:[10.1086/508454](https://doi.org/10.1086/508454).

- [14] Chen, F., Zhou, Y., 2011. Attractivity of fractional functional differential equations. *Computers & Mathematics with Applications* 62, 1359–1369. doi:[10.1016/j.camwa.2011.03.062](https://doi.org/10.1016/j.camwa.2011.03.062).
- [15] Chen, Z.M., Dong, B.Q., Zhang, Q., 2025. l^2 decay estimates of weak solutions to 3D fractional MHD equations in exterior domains. doi:[10.48550/ARXIV.2501.17179](https://doi.org/10.48550/ARXIV.2501.17179).
- [16] Das, S., 2011. *Functional Fractional Calculus*. Springer Berlin Heidelberg. doi:[10.1007/978-3-642-20545-3](https://doi.org/10.1007/978-3-642-20545-3).
- [17] Davidson, P.A., 2001. *An Introduction to Magnetohydrodynamics*. Cambridge University Press. doi:[10.1017/cbo9780511626333](https://doi.org/10.1017/cbo9780511626333).
- [18] Fambri, F., Sonnendrücker, E., 2025. Structure preserving hybrid finite volume finite element method for compressible mhd. *Journal of Computational Physics* 523, 113691. doi:[10.1016/j.jcp.2024.113691](https://doi.org/10.1016/j.jcp.2024.113691).
- [19] Feng, W., Sun, S., Han, Z., Zhao, Y., 2011. Existence of solutions for a singular system of nonlinear fractional differential equations. *Computers & Mathematics with Applications* 62, 1370–1378. doi:[10.1016/j.camwa.2011.03.076](https://doi.org/10.1016/j.camwa.2011.03.076).
- [20] Grauer, R., Marliani, C., 1998. Geometry of singular structures in magnetohydrodynamic flows. *Physics of Plasmas* 5, 2544–2552. doi:[10.1063/1.872939](https://doi.org/10.1063/1.872939).
- [21] He, Y., Zou, J., 2018. A priori estimates and optimal finite element approximation of the MHD flow in smooth domains. *ESAIM: Mathematical Modelling and Numerical Analysis* 52, 181–206. doi:[10.1051/m2an/2018006](https://doi.org/10.1051/m2an/2018006).
- [22] Hiptmair, R., Pagliantini, C., 2018. Splitting-based structure preserving discretizations for magnetohydrodynamics. *The SMAI Journal of computational mathematics* 4, 225–257. doi:[10.5802/smai-jcm.34](https://doi.org/10.5802/smai-jcm.34).
- [23] Jadhav, K., Chandy, A.J., 2021. Analysis of energy transfer through direct numerical simulations of magnetohydrodynamic Orszag–Tang vortex. *Physics of Fluids* 33. doi:[10.1063/5.0051476](https://doi.org/10.1063/5.0051476).
- [24] John, V., Linke, A., Merdon, C., Neilan, M., Rebholz, L.G., 2017. On the divergence constraint in mixed finite element methods for incompressible flows. *SIAM Review* 59, 492–544. doi:[10.1137/15m1047696](https://doi.org/10.1137/15m1047696).
- [25] Kayanikhoo, F., Cemeljic, M., Wielgus, M., Kluzniak, W., 2023. Energy dissipation in astrophysical simulations: results of the Orszag–Tang test problem. doi:[10.48550/ARXIV.2312.06675](https://doi.org/10.48550/ARXIV.2312.06675).
- [26] Khan, M., Zhang, Z., Lu, D., 2023. Numerical simulations and modeling of MHD boundary layer flow and heat transfer dynamics in Darcy–Forchheimer media with distributed fractional-order derivatives. *Case Studies in Thermal Engineering* 49, 103234. doi:[10.1016/j.csite.2023.103234](https://doi.org/10.1016/j.csite.2023.103234).
- [27] Li, N., Wang, X., Xu, H., Qi, H., 2024. Numerical study on radiative MHD flow of viscoelastic fluids with distributed-order and variable-order space fractional operators. *Mathematics and Computers in Simulation* 215, 291–305. doi:[10.1016/j.matcom.2023.07.021](https://doi.org/10.1016/j.matcom.2023.07.021).
- [28] Liao, H.I., McLean, W., Zhang, J., 2019. A discrete Grönwall inequality with applications to numerical schemes for subdiffusion problems. *SIAM Journal on Numerical Analysis* 57, 218–237. doi:[10.1137/16m1175742](https://doi.org/10.1137/16m1175742).

- [29] Liu, H., Zheng, X., Fu, H., 2022. Analysis of a multi-term variable-order time-fractional diffusion equation and its Galerkin finite element approximation. *Journal of Computational Mathematics* 40, 814–834. doi:[10.4208/jcm.2102-m2020-0211](https://doi.org/10.4208/jcm.2102-m2020-0211).
- [30] Liu, Y., Jiang, M., 2024. Magnetohydrodynamic analysis and fast calculation for fractional Maxwell fluid with adjusted dynamic viscosity. *Magnetochemistry* 10, 72. doi:[10.3390/magnetochemistry10100072](https://doi.org/10.3390/magnetochemistry10100072).
- [31] Liu, Y., Jiang, X., Jia, J., 2024. Numerical simulation and parameter estimation of the space-fractional magnetohydrodynamic flow and heat transfer coupled model. *Fractal and Fractional* 8, 557. doi:[10.3390/fractalfract8100557](https://doi.org/10.3390/fractalfract8100557).
- [32] Madiyarov, M., Alimbekova, N., Bakishev, A., Mukhamediyev, G., Yergaliyev, Y., 2025. Nonlocal modeling and inverse parameter estimation of time-varying vehicular emissions in urban pollution dynamics. *Mathematics* 13, 2772. doi:[10.3390/math13172772](https://doi.org/10.3390/math13172772).
- [33] Magin, R.L., 2004. Fractional calculus in bioengineering, part 1. *Critical Reviews in Biomedical Engineering* 32, 1–104. doi:[10.1615/critrevbiomedeng.v32.10](https://doi.org/10.1615/critrevbiomedeng.v32.10).
- [34] Mainardi, F., 2010. *Fractional Calculus and Waves in Linear Viscoelasticity: An Introduction to Mathematical Models*. Imperial College Press. doi:[10.1142/p614](https://doi.org/10.1142/p614).
- [35] Malaikah, H., Al-Abdali, J.F., 2025. Variable-order fractional derivatives in financial systems. *Applied Mathematics* 16, 461–469. doi:[10.4236/am.2025.166025](https://doi.org/10.4236/am.2025.166025).
- [36] Metzler, R., Klafter, J., 2000. The random walk’s guide to anomalous diffusion: a fractional dynamics approach. *Physics Reports* 339, 1–77. doi:[10.1016/s0370-1573\(00\)00070-3](https://doi.org/10.1016/s0370-1573(00)00070-3).
- [37] Mohamad, A., Viskanta, R., 1993. Modeling of turbulent buoyant flow and heat transfer in liquid metals. *International Journal of Heat and Mass Transfer* 36, 2815–2826. doi:[10.1016/0017-9310\(93\)90101-b](https://doi.org/10.1016/0017-9310(93)90101-b).
- [38] Moreau, R., 1990. *Magnetohydrodynamics*. Springer Netherlands. doi:[10.1007/978-94-015-7883-7](https://doi.org/10.1007/978-94-015-7883-7).
- [39] Motsa, S.S., Shateyi, S., Marewo, G.T., Sibanda, P., 2011. An improved spectral homotopy analysis method for MHD flow in a semi-porous channel. *Numerical Algorithms* 60, 463–481. doi:[10.1007/s11075-011-9523-0](https://doi.org/10.1007/s11075-011-9523-0).
- [40] Orszag, S.A., Tang, C.M., 1979. Small-scale structure of two-dimensional magnetohydrodynamic turbulence. *Journal of Fluid Mechanics* 90, 129–143. doi:[10.1017/s002211207900210x](https://doi.org/10.1017/s002211207900210x).
- [41] Planas, R., Badia, S., Codina, R., 2011. Approximation of the inductionless mhd problem using a stabilized finite element method. *Journal of Computational Physics* 230, 2977–2996. doi:[10.1016/j.jcp.2010.12.046](https://doi.org/10.1016/j.jcp.2010.12.046).
- [42] Qiao, Y., Xu, H., Qi, H., 2024. Rotating MHD flow and heat transfer of generalized Maxwell fluid through an infinite plate with Hall effect. *Acta Mechanica Sinica* 40. doi:[10.1007/s10409-023-23274-x](https://doi.org/10.1007/s10409-023-23274-x).
- [43] Rehman, A.U., Hua, S., Riaz, M.B., Awrejcewicz, J., Xiange, S., 2023. A fractional study with Newtonian heating effect on heat absorbing MHD radiative flow of rate type fluid with application of novel hybrid fractional derivative operator. *Arab Journal of Basic and Applied Sciences* 30, 482–495. doi:[10.1080/25765299.2023.2250063](https://doi.org/10.1080/25765299.2023.2250063).

- [44] Roberts, P.H., King, E.M., 2013. On the genesis of the Earth's magnetism. *Reports on Progress in Physics* 76, 096801. doi:[10.1088/0034-4885/76/9/096801](https://doi.org/10.1088/0034-4885/76/9/096801).
- [45] Shakeri, F., Dehghan, M., 2011. A finite volume spectral element method for solving magnetohydrodynamic (MHD) equations. *Applied Numerical Mathematics* 61, 1–23. doi:[10.1016/j.apnum.2010.07.010](https://doi.org/10.1016/j.apnum.2010.07.010).
- [46] Shen, M., Chen, S., Liu, F., 2018. Unsteady MHD flow and heat transfer of fractional Maxwell viscoelastic nanofluid with Cattaneo heat flux and different particle shapes. *Chinese Journal of Physics* 56, 1199–1211. doi:[10.1016/j.cjph.2018.04.024](https://doi.org/10.1016/j.cjph.2018.04.024).
- [47] Shiyapov, K., Abdiramanov, Z., Issa, Z., Zhumaseyitova, A., 2026. High-order spectral scheme with structure maintenance and fast memory algorithm for nonlocal nonlinear diffusion equations. *AppliedMath* 6, 54. doi:[10.3390/appliedmath6040054](https://doi.org/10.3390/appliedmath6040054).
- [48] Sun, H.G., Chang, A., Zhang, Y., Chen, W., 2019. A review on variable-order fractional differential equations: Mathematical foundations, physical models, numerical methods and applications. *Fractional Calculus and Applied Analysis* 22, 27–59. doi:[10.1515/fca-2019-0003](https://doi.org/10.1515/fca-2019-0003).
- [49] Tarasov, V.E., 2010. *Fractional Dynamics: Applications of Fractional Calculus to Dynamics of Particles, Fields and Media*. Springer Berlin Heidelberg. doi:[10.1007/978-3-642-14003-7](https://doi.org/10.1007/978-3-642-14003-7).
- [50] Vaz, J., de Oliveira, E.C., 2025. On fractional differential equations, dimensional analysis, and the double gamma function. *Nonlinear Dynamics* 113, 34305–34320. doi:[10.1007/s11071-025-11386-8](https://doi.org/10.1007/s11071-025-11386-8).
- [51] Beirão da Veiga, L., Dassi, F., Vacca, G., 2025. Pressure and convection robust finite elements for magnetohydrodynamics. *Numerische Mathematik* 157, 1161–1209. doi:[10.1007/s00211-025-01476-5](https://doi.org/10.1007/s00211-025-01476-5).
- [52] Wacker, B., Arndt, D., Lube, G., 2016. Nodal-based finite element methods with local projection stabilization for linearized incompressible magnetohydrodynamics. *Computer Methods in Applied Mechanics and Engineering* 302, 170–192. doi:[10.1016/j.cma.2016.01.004](https://doi.org/10.1016/j.cma.2016.01.004).
- [53] Zhao, J., Zheng, L., Zhang, X., Liu, F., 2016. Convection heat and mass transfer of fractional MHD Maxwell fluid in a porous medium with Soret and Dufour effects. *International Journal of Heat and Mass Transfer* 103, 203–210. doi:[10.1016/j.ijheatmasstransfer.2016.07.057](https://doi.org/10.1016/j.ijheatmasstransfer.2016.07.057).